Configuration and validation of an oceanic physical and biogeochemical model to investigate coastal eutrophication: case study in the Southern California Bight

Fayçal Kessouri[1], Karen McLaughlin[1], Martha Sutula [1], Daniele Bianchi[2], Minna Ho[1], James C McWilliams [2], Lionel Renault[2,3], Jeroen Molemaker[2], Curtis Deutsch[4], Anita Leinweber[2]

[1]Southern California Coastal Water Research Project, Costa Mesa, CA [2]Department of Atmospheric and Oceanic Sciences, University of California Los Angeles, CA [3]Laboratoire d'Études en Géophysique et Océanographie Spatiale, Toulouse, France [4]School of Oceanography, University of Washington, WA

Key Points:

- The model allows to disentangle natural variability, climate change, and local anthropogenic forcing.
- The model reproduces the gradients of physical and biogeochemical properties that can be traced to the influence of coastal inputs.
- The model reproduces nutrient enrichment via subsurface wastewater outfall plumes and riverine runoff.

Corresponding author: F. Kessouri and K. McLaughlin, `faycalk@sccwrp.org` ; `karenm@sccwrp.org`

Abstract

The Southern California Bight (SCB), an eastern boundary upwelling system, is impacted by global warming, acidification and deoxygetation, and receives anthropogenic nutrients from a coastal population of 20 million people. We describe the configuration, forcing, and validation of a realistic, submesoscale resolving ocean model as a tool to investigate coastal eutrophication. This modeling system represents an important achievement because it strikes a balance of capturing the forcing by U.S. Pacific Coast-wide phenomena, while representing the bathymetric features and submesoscale circulation that affect the vertical and horizontal transport of nutrients from natural and human sources. Moreover, the model allows to run simulations at timescales that approach the interannual frequencies of ocean variability, making the grand challenge of disentangling natural variability, climate change, and local anthropogenic forcing a tractable task in the near-term. The model simulation is evaluated against a broad suite of observational data throughout the SCB, showing realistic depiction of mean state and its variability with remote sensing and in situ physical-biogeochemical measurements of state variables and biogeochemical rates. The simulation reproduces the main structure of the seasonal upwelling front, the mean current patterns, the dispersion of plumes, as well as their seasonal variability. It reproduces the mean distributions of key biogeochemical and ecosystem properties. Biogeochemical rates reproduced by the model, such as primary productivity and nitrification, are also consistent with measured rates. Results of this validation exercise demonstrate the utility of fine-scale resolution modeling in support of management decisions on local anthropogenic nutrient discharges to coastal zones.

Plain Language Summary

We applied and validated an ocean numerical model to investigate the effects of land-based and atmospheric nutrient loading on coastal eutrophication and its effects on carbon, nitrogen and oxygen cycles of the Southern California Bight, an upwelling-dominated marine embayment on the U.S. West Coast. The model is capable of high resolution, multi-year hindcast simulations, which permits mechanistic investigations to disentangle natural variability, climate change, and local human pressures that accelerate land-based and atmospheric nitrogen and phosphorus loads. The model performance assessment illustrates that it faithfully reproduces the monitored ocean state properties related to algal blooms, oxygen and pH, among others, that can be traced to the influence of human influences on land-based and atmospheric inputs of nutrients and carbon. The model performance assessment helps to constrain uncertainties in predictions to support ongoing conversations on approaches to mitigate climate change, including considerations of management of local nutrient and carbon inputs.

1 Introduction

Human-driven eutrophication has resulted in profound impacts to coastal ecosystems around the world. These impacts are arguably the best studied in estuaries and enclosed bays (e.g. Chesapeake Bay; Cerco & Cole, 1993; Boesch, Brinsfield, & Magnien, 2001) and semi-enclosed seas such as the Baltic Sea (Savchuk & Wulff, 2007; Cederwall & Elmgren, 1990), the Mediterranean Sea (Arhonditsis et al., 2000), and the Gulf of Mexico (Justić et al., 2005; Laurent et al., 2018). To date, few investigations of coastal eutrophication have occurred in Eastern Boundary Upwelling systems (EBUS). While strong upwelling and vigorous surface currents would generally limit the extent to which coastal eutrophication could occur (Fennel & Testa, 2019), such investigations have also been limited by coupled physical biogeochemical numerical modeling approaches that can adequately resolve fine-resolution bathymetry and the complexities of submesoscale circulation (McWilliams, 2016; Dauhajre et al., 2019), while simulating a sufficient duration (several years) to distinguish oceanic versus terrestrial forcing. These submesoscale circulation features, including fine

scale eddies and filaments $< 5\,\text{km}$ in horizontal resolution, strongly control the magnitude and variability of nearshore upwelling and associated nutrient transport. Thus, high resolution, submesoscale-resolving numerical models are a necessary prerequisite for mechanistic modeling studies and source attribution of oceanic versus terrestrial drivers of coastal eutrophication in EBUS. Inadequate modeling system and lack of numerical model validation have been identified as significant barriers to effective, evidence-based solutions to coastal eutrophication (Boesch, 2019).

All the necessary ingredients are present to motivate a numerical modeling investigation of the role of coastal eutrophication in driving ocean acidification and deoxygenation in the Southern California Bight (SCB), a large marine open embayment found in the California Current System (CCS) on the U.S. Pacific Coast. First, the SCB is a biologically-productive region, and thus of high economic and ecological importance. Seasonal upwelling of nutrient-rich deep water maintains high rates of biological productivity over broad scales. At the same time, upwelling draws water masses that are naturally low in dissolved oxygen (DO), pH, and carbonate saturation state (Ω_{Ar}) onto the shelf and into the photic zone (Sutton et al., 2017). Second, the SCB has one of the most spatially comprehensive and longest-running coastal observational systems in the world. Several physical and biogeochemical variables are sampled regularly and extensively, creating an ideal setting for model-data comparisons. Third, the SCB is home to one of the most densely populated coastal regions in North America, where the discharges of primary or secondary treated wastewater from a population of 20 million people are released to the coastal zone via ocean outfalls, along with the urban and agricultural runoff from 72 rivers. These nutrient sources rival natural upwelling in magnitude (Howard et al., 2014), roughly doubling available nitrogen to nearshore coastal waters. Intensifying ocean acidification and deoxygenation and harmful algal blooms have motivated California policy makers to consider reducing anthropogenic nutrients as a climate change mitigation strategy (Ocean Acidification Action Plan 2016), but wastewater treatment plant upgrades and non-point source controls would cost billions. A numerical modeling approach is needed to disentangle the effects of natural upwelling and climate change from anthropogenic nutrient loading from land-based and atmospheric sources.

To support such investigations, the regional oceanic model system (ROMS, Shchepetkin & McWilliams, 2005) coupled to the biogeochemical elemental cycling model (BEC, Moore, Doney, & Lindsay, 2004) has been recently adapted for the CCS (Renault, McWilliams, et al., 2020; Deutsch et al., 2020). A nested model domain was established, scaling from 4-km (horizontal) resolution CCS-wide, one $1\,\text{km}$ horizontal resolution nest covering California nearshore, then to a 0.3 km nest in the Southern California Bight (SCB), where investigations of local anthropogenic inputs were focused. Modeling experiments investigating submesoscale transport (captured at model resolutions ≤ 1 km) have demonstrated an up to ten-fold increase in the magnitude of vertical N fluxes relative to mesoscale transport represented by a 4 km model (Capet et al., 2008). furthermore, a finer horizontal resolution of bathymetry improves the representation of coastal currents, submesoscale circulation, and coast-offshore connectivity (Dauhajre et al., 2019). For this reason, investigations of coastal eutrophication are simulated at 0.3 km resolution. Simulations conducted at the $4\,\text{km}$ ROMS-BEC model domain have been validated for regional-scale atmospheric forcing, physics, and biogeochemistry, including O_2, carbonate saturation state, primary productivity, and hydrographic parameters, demonstrating that the model captures broad patterns of critical properties in the CCS (Renault, McWilliams, et al., 2020; Deutsch et al., 2020). However, additional focused validation of nearshore, anthropogenically-enhanced gradients in nutrients, primary production, oxygen and pH in model simulations conducted at 0.3 km resolution are needed to gauge model utility to investigate the role of coastal eutrophication in impacting ocean acidification and deoxygenation.

We employed this dynamically downscaled, submesoscale-resolving physical-biogeochemical model to investigate the effects of land-based and atmospheric nutrient inputs in driv-

ing coastal eutrophication and ocean acidification and deoxygenation. The aim of this manuscript is to: 1) document the SCB ROMS-BEC model configuration, including the effects of land-based and atmospheric inputs of nutrients and organic carbon, intended to support investigations of coastal eutrophication, and 2) present a validation of SCB ROMS-BEC simulations against available observations, focusing on anthropogenically-enhanced gradients in nutrient, primary production, oxygen, and pH.

2 SCB coupled physical and biogeochemical model description, configuration and forcing

2.1 Model description

A detailed description of the ROMS-BEC configuration used in this paper can be found in Renault, McWilliams, et al., 2020; Deutsch et al., 2020. We refer the reader to these papers for a discussion of the model setup, boundary forcing, and main equations.

The ROMS physical model (Shchepetkin & McWilliams, 2005) is widely-used, open-source code that solves the hydrostatic, free-surface primitive equations in 3-D curvilinear coordinates. It contains state-of-art, numerical algorithms that provide an accurate and stable representation of physical processes down to scales of meters, and allow for "nesting" of high-resolution sub-domains within larger domains. ROMS has been validated for the CCS (e.g. see Renault, Molemaker, et al., 2016; Renault, McWilliams, et al., 2020).

This hindcast model has been successfully run over a decadal using high-resolution spatial and temporal atmospheric forcing that resolve the effects of wind drop-off, the current feedback on the surface stress (Renault, Molemaker, et al., 2016), and high-frequency wind fluctuations (Renault, Molemaker, et al., 2016).

To provide a representation of biogeochemical cycles, ROMS is dynamically coupled to the BEC model (Moore et al., 2004; Gruber, 2004; Gruber et al., 2011). Ocean biogeochemical modeling approaches can have a broad range of complexities, ranging from few functional groups (e.g. NPZD models, Fasham, 1993), to multiple biogeochemical cycles (e.g. C, N, O) and plankton functional groups. BEC is a multi-element (C, N, P, O, Fe, Si) and multiplankton model that includes three phytoplankton functional groups (picoplankton, silicifying diatoms, and N-fixing diazotrophs), one zooplankton group, and dissolved and sinking organic detritus. As such, it models lower ecosystem trophic interactions at an intermediate level of ecosystem complexity, relative to other marine ecosystem models such as PISCES (Aumont & Bopp, 2006), NEMURO (Aita et al., 2007) and PlankTOM5 (Buitenhuis et al., 2012). Despite its relative simplicity, BEC exhibits good model skill in predicting net primary production (Laufkötter et al., 2015), which is key to linking coastal eutrophication to ocean acidification and deoxygenation. The BEC model was expanded to provide a better resolution of N, C, alkalinity, Fe, and O_2 cycling (Deutsch et al., 2020). These innovations include an improved nitrogen cycle representation that tracks nitrate, nitrite, ammonium and nitrous oxide species, and the microbially-mediated N transformations that connect them (Foster et al., 2011). The ecosystem is linked to a C system module that tracks dissolved inorganic carbon (DIC) and alkalinity, and an air-sea gas exchange module that allows realistic representation of dissolved gases (e.g. O_2, CO_2 and nitrous oxide), based on the formulation of Wanninkhof, 1992.

2.2 Model configuration

The SCB model domain extends along a 450 km stretch of the coast, from Tijuana to Pismo Beach, and about 200 km offshore. This grid, shown in Fig. 1, is composed of 1400 x 600 grid-points, with a nominal resolution of dx = 0.3 km. The grid uses the stretching parameters: $\theta_s = 6.$, $\theta_b = 3.$ and $hc = 250$ m, and a time step of 30 seconds. The model
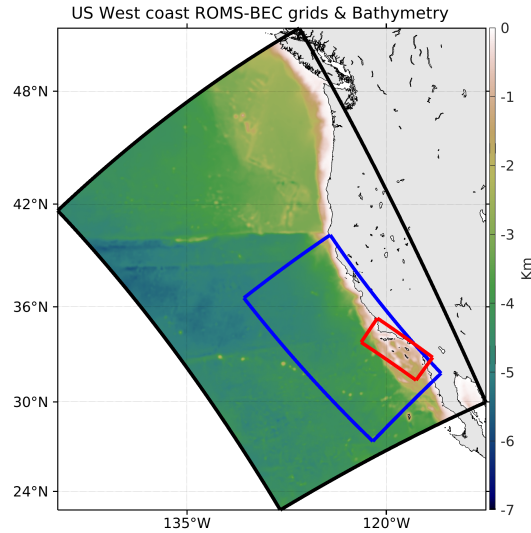
Figure 1: ROMS-BEC model configurations. dx=4km is the black box, dx=1km is the blue box, dx=0.3km is the red box. Background is the topography from dx=4km.

configuration has $60\,\sigma$-coordinate vertical levels using the stretching function described in Shchepetkin & McWilliams, 2009. Output is saved as 1-day averages.

The oceanic forcing of the 0.3 km domain originates from multi-level nesting. A 4 km simulation is initialized and forced at the open boundaries by a pre-existing North-east Pacific-wide ROMS solution at 12 km resolution (Renault, McWilliams, et al., 2020), and is run for the period 1995-2010, after a spin-up of 2 years. A 1 km simulation is initialized and forced from the 4 km model, starting in October 1996 and ending in December 2007. The 0.3 km simulation is initialized and forced at its boundaries by the 1 km simulation starting from January 1997 and ending in December 2000. The bathymetry used in this configuration comes from the Southern California Coastal Oceanic Observation System (SCCOOS) 3 Arc-Second Coastal Relief Model Development (90 m horizontal resolution).

The model configuration is forced by hourly outputs from an atmospheric simulation with the Weather Research and Forecast model (WRF06; Skamarock & Klemp, 2008) run at 6 km resolution over a domain similar to the 4 km (Fig. 1 and used for Renault, Hall, & McWilliams, 2016), and includes a wind-current coupling parameterization necessary to attain more realistic simulations of the oceanic eddy kinetic energy (EKE) and circulation (Renault, Molemaker, et al., 2016; Renault, Masson, et al., 2020).

Model simulations were conducted from 1997-2000, a period chosen to capture the effects of all three phases of the El Niño–Southern Oscillation (ENSO); it also captures the beginning of the "modern" state of point source management in the SCB, where several major POTWs were in transition from primary to secondary treatment.

2.3 Terrestrial and atmospheric forcing of freshwater, nutrients and carbon

Model simulations were forced with a monthly time series of spatially-explicit input parameters, including freshwater flow, nitrogen, phosphorus, silica, and organic carbon rep-

resenting natural and anthropogenic sources. These data have been compiled from POTW ocean outfalls and riverine discharges (1996-2013) and spatially explicit modeled estimates of atmospheric deposition. POTW effluent data were compiled from permit monitoring databases. Database records from Orange County Sanitation District (OCSD) outfall effluent only included ammonium, and, as a result, nitrate was estimated from 2008 effluent concentrations, which, based on more recent work, may underestimate the total nitrogen load by 10 - 15%. Monthly time series of surface water runoff from 72 rivers are from model simulations and monitoring data. Direct atmospheric deposition is derived from the Community Multi-scale Air Quality model (Byun et al., 2006), and follows the implementation of Deutsch et al., 2020. In this paper, we discuss in detail the formulation of the river and wastewater outfall inputs.

2.4 Configuration of river and wastewater outfall forcing in ROMS-BEC

Ocean outfalls and coastal rivers are modeled as mass sources into the ocean. To accomplish this, we add explicit volume fluxes to the otherwise divergence-free flow in the ocean. The inclusion of these fluxes makes it possible to account for associated sources of tracers, while satisfying conservation laws. Specifically, our approach allows for the proper influx of fresh water in the ocean, without resorting to a 'virtual salt' flux, which is a common approach in larger scale ocean models (Kang et al., 2017). Since we explicitly include known volume fluxes for both rivers and outfall pipes, specification of tracer concentration is sufficient to correctly model the source terms. The tracer evolution equations that are used in ROMS are implemented by using control volumes (Shchepetkin & McWilliams, 2005) where for each tracer concentration C,

$$\frac{\partial \iiint C \, dV}{\partial t}(x, y, z, t) = \iint u_n C \, dA(x, y, z, t) + \text{mixing}. \tag{1}$$

where V is the control volume and u_n the normal velocity into the volume. Additionally, we enforce mass conservation which implies;

$$\frac{\partial V}{\partial t}(x, y, z, t) = \iint u_n \, dA(x, y, z, t). \tag{2}$$

In absence of rivers and outfalls, the flow is volume conservative, and the integral on the right hand side of equation (2) is identical zero. Using eqs. (1) and (2), it is easy to see that the mean concentration of a tracer can be lowered if the average concentration of the flux entering the control volume is less than the mean concentration in that volume. In this manner, fresh water rivers will lower the salinity of the water in which they enter. All 72 rivers and 18 POTW pipes that are considered in this study are implemented in this manner.

Each individual source is based on the following equation (with the subscript i omitted for convenience):

$$S(x, y, z, t) = \frac{W(x, y, z) \, Q_s(t) \, C_s(t)}{V_s} \tag{3}$$

With:

$S(x, y, z, t)$: volume source of contaminant (mmol m^{-3} s^{-1}).

$W(x, y, z)$: non-dimensional shape function (with values between 0 and 1).

$Q_s(t)$: water volume flux from the source (m^3 s^{-1}).

$C_s(t)$: concentration of the tracer C in the source water (mmol m^{-3}).

V_s: effective volume of the source (m^3).

For each source, $Q_s(t)$ and $C_s(t)$ are prescribed as time series. The shape function $W(x, y, z)$ distributes the tracer in the water column, representing non-resolved mixing and dilution effects. Its values represent the relative intensity of the *in situ* tracer injection, with

values between 0 and 1. The effective 3D volume of the source is calculated from the shape function $W(x, y, z)$ as:

$$V_s = \iiint W(x, y, z) \, dV \tag{4}$$

where the integral is over the model domain. For convenience, we assume that $W(x, y, z)$ can be separated into a horizontal shape function $A(x, y)$, multiplied by a vertical shape function $H(z)$ (both non-dimensional and with values between 0 and 1), such that:

$$V_s = \iint A(x, y) \, dx \, dy \int H(z) dz = A_s \, H_s \tag{5}$$

Here, A_s represents the effective source surface area (m^2), and H_s the effective source thickness (m). The functions $A(x, y)$ and $H(z)$ are defined differently for POTW and rivers. They are assumed to be fixed in time; a time-dependent generalization (for example to mimic variations in the depth of the POTW buoyant plume) is straightforward. For POTW inputs, at each main diffuser, the horizontal distribution $A(x, y)$ of the source is shown in Fig. 2. This method of weighting the plume in different cells allows the effluent to be diluted and prevents the model from developing numerical instabilities. The flow is divided in two at Hyperion (Fig. 2A) and PLWTP (Fig. 2D) to account for their Y-shaped diffuser, partitioning 50% of the flow to each diffuser. OCSD (Fig. 2C) has one flow through its L-shaped diffuser. JWPCP (Fig. 2B) has three diffusers, the Y-shape northern get 17.5% of the flow for each leg of the Y-diffuser, and the southern L-shape diffuser gets 65% of the flow. The vertical profile of the POTW sources is defined by a Gaussian function centered at a height z above the bottom (h_b), to mimic a buoyant plume, so that $H(z)$ is given by:

$$H(z) = e^{-z^2/d_s^2} \tag{6}$$

Where $z = -h_b + h_s$, with

h_b: bottom depth (m).

h_s: depth of the buoyant plume above the bottom (m).

d_s: vertical scale of the POTW plume (m).

We further assume $h_s = 20$ m and $d_s = 10$ m, as in Uchiyama, Idica, McWilliams, & Stolzenbach, 2014.

We distribute the SCB rivers on one horizontal grid point (0.3 km wide), where we assume $A(x, y) = 1$, and similarly distribute the source vertically, with the Gaussian function centered at the surface. h_s here is simply the water column depth to put the maximum input at the surface. Because in ROMS the thickness of vertical grid cells varies in time, to ensure tracer conservation the calculation of the input source volume V_s must be done at each time step, even in the case of a time-independent source shape function $W(x, y, z)$. Effectively, only $H_s = H(z)$ needs to be recalculated at each time step.

3 Model performance assessment approach

The conceptual approach for model performance assessment is comprised of three components, addressing different aspects of skill assessment: 1) statistical comparison of model output to observational data for state variables by region and season; 2) comparison of model output to observational data for biogeochemical rates; 3) evaluation of model behavior compared to expected biogeochemical dynamics for coastal zones. Comparison of model output to observational data by region and season is designed to document model skill at reproducing the statistics (e.g. mean values and variability) of ocean physical and biogeochemical parameters at the spatio-temporal scales more relevant for evaluating human impacts on the coastal environment. Comparison of model output to observational data for biogeochemical rates assures that model is capturing the appropriate transformations in nutrients and carbon that structure the ecosystem response to eutrophication. Finally, the evaluation of model behavior compared to the expected physical and biogeochemical dynamics for coastal zones is a more qualitative evaluation of model performance to document that the model
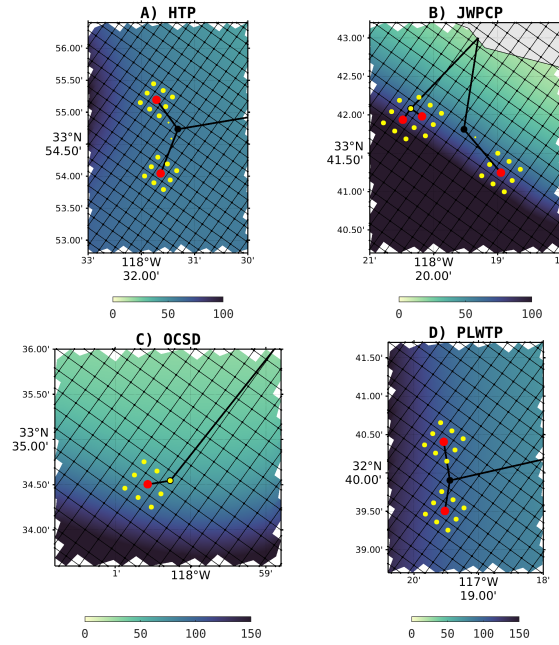
Figure 2: Spatial distribution of the point sources to simulate and to dilute the freshwater, nutrients and organic matter fluxes for the 4 majors POTW underwater outfalls locations.

broadly reproduces oceanographic phenomena in a way that reflects our understanding of nearshore ocean environments.

3.1 Description of Observational Datasets

3.1.1 Ship-Based Ocean Monitoring

The SCB is home to a suite of long-running monitoring programs that make it one of the best observed coastal ecosystems in the world. Among them, the California Coopera-tive Oceanic Fisheries Investigations (CalCOFI) program (McClatchie, 2016), initiated in the 1950s, samples the SCB quarterly each year, collecting hydrographic and biogeochem-ical measurements in coordination with the Southern California Coastal Ocean Observing System (SCCOOS). These observations are augmented nearshore by quarterly surveys of nearshore water column and benthic parameters conducted collaboratively since 1990 by POTW agencies as a part of their regulatory monitoring requirements (Howard et al., 2014; McLaughlin et al., 2018; Booth et al., 2014; Nezlin et al., 2018). These programs provide good temporal and geographical coverage of both the offshore (CalCOFI) and nearshore (POTW) areas, coinciding with the model period, and include publicly available water qual-ity data for targeted sites measured quarterly. We validated model output against observed temperature, dissolved oxygen, nitrate, ammonium, chlorophyll, carbon-system parameters (pH and aragonite saturation state), primary production, and nitrification.

In situ measurements have inherent uncertainty, due to a combination of measurement sensitivity and sampling frequency and intensity, making them an imperfect "truth" with which to compare to model output. However, this uncertainty is not the same for all param-eters. Both temperature and dissolved oxygen are collected using high resolution probes,

though the two programs used in this study incorporate slightly different calibration protocols for dissolved oxygen, lending greater confidence to data-model comparisons for these datasets. Chlorophyll is measured on discrete bottle samples in the CalCOFI program, a high quality measurement, but inferred from *in situ* fluorescence measurements in the POTW monitoring program, adding uncertainty to these measurements. Nitrate and ammonium concentrations are measured on discrete bottle samples for both programs, but the detection limits are more sensitive in the CalCOFI program. Furthermore, nutrients are not measured with the same sampling density in POTW monitoring programs as sensor data. Similarly, primary production is measured at a subset of locations in the CalCOFI program and as a short-term special study in Southern California Bight Regional Marine Monitoring Program (Bight Program). Details on measurements and sample collection protocols for the CalCOFI program can be found on their website (www.CalCOFI.org; McClatchie, 2016) and for the POTW monitoring programs in Howard et al., 2014. The map of all monitoring stations used in this study can be found in the Supporting Information, Fig. 22). The data could be found in Kessouri, McLaughlin, et al., 2020.

3.1.2 Remote sensing observations

Satellite ocean color measurements for chlorophyll were used to characterize horizontal gradients at finer scales than possible with the ship-based monitoring. We use monthly averaged surface chlorophyll concentration from the period 1997 to 2000 derived from the SeaWiFS sensor at 4 km spatial resolution. Large gaps in the dataset can occur because of dense cloud cover that occurs in late spring and early summer. Despite the limitations, satellite data provide a valuable representation of the spatial distribution of chlorophyll and temperature at seasonal scales over the region.

3.2 Performance Statistics

Our approach to a statistical assessment of agreement between model predictions versus observations reflect the fact that the hydrodynamic model, under the influence of realistic forcings (e.g. wind fields) and without data assimilation, develops its own intrinsic variability in circulation, e.g. submesoscale eddies (McWilliams, 2007). The resulting modeled state variables would not necessarily overlap with observations on a point-by-point basis, but would be comparable to observations when averaged over appropriate spatio-temporal scales. We assessed a suite of statistics and metrics, following the methodology of Allen, Somerfield, & Gilbert, 2007 to assess how well the model reproduces the magnitude and gradients of selected state variables, whether the model agreement has an apparent bias, and how well the model reproduces natural variability. We calculated six metrics, defined in the following, where N is the total number of appropriate observational data, D represents each individual observational datum, $\overline{D}$ is the mean of the observational data, M is the model estimate representing an observation, and $\overline{M}$ is the mean of the model estimate. The metrics considered include:

The Pearson correlation coefficient, reflecting the degree of linear correlation between the observed and model variable, and the statistical significance (p-value) of this correlation:

$$r_{xy} = \frac{\sum_{n=1}^{N}(D_n - \overline{D})(M_n - \overline{M})}{\sqrt{\sum_{n=1}^{N}(D_n - \overline{D})^2}\sqrt{\sum_{n=1}^{N}(M_n - \overline{M})^2}}; \tag{7}$$

The Cost Function (CF), which gives a non-dimensional value indicative of the "goodness of fit" between two sets of data, quantifying the difference between model results and measurement data:

$$\text{CF} = \frac{1}{N}\sum_{n=1}^{N}\frac{|D_n - M_n|}{\sigma_D} \tag{8}$$

where σ_D is the standard deviation of the observations;

The Percentage Bias (PB) (the sum of model error normalized by the data):

$$\text{PB} = \frac{\sum(D - M)}{\sum D} * 100; \tag{9}$$

The Ratio of the Standard Deviations (RSD):

$$\text{RSD} = \frac{\sigma_D}{\sigma_M} \tag{10}$$

where σ_M is the standard deviation of model outputs;

The Nash-Sutcliffe Model Efficiency (ME), (Nash and Sutcliffe, 1970) a measure of the ratio of the model error to the variability of the data:

$$\text{ME} = 1 - \frac{\sum(D_n - M_n)^2}{\sum(D - \overline{D})}; \tag{11}$$

And the two-sample t-test, or Welch's t-test:

$$t = (\overline{D} - \overline{M})/\sqrt{\frac{\sigma_D^2}{N} + \frac{\sigma_M^2}{N}}. \tag{12}$$

We score the model performance following Table 1 per the methodology of Allen et al., 2007.

Statistic	Excellent	Good	Reasonable	Poor
Cost Function (Commission et al., 1998)	<1	1-2	2-5	>5
Cost Function (Moll & Radach, 2003)	<1	1-2	2-3	>3
Nash Sutcliff Model Efficiency (Maréchal, 2004)	>0.65	0.65-0.5	0.5-0.2	<0.2
Percentage Bias (Maréchal, 2004)	<|0.1|	|0.1-0.2|	|0.2-0.4|	>|0.4|
H	0			1
Correlation Coefficient	1-0.9	0.9-0.8	0.8-0.6	<0.6
p-value	<0.05			>0.05
Ratio of Standard Deviations	1-0.9,1-1.1	0.9-0.8, 1.1-1.2	0.8-0.6, 1.2-1.4	<0.6, >1.4

Table 1: Model performance

4 Model performance assessment findings

4.1 Ocean circulation

The SCB is situated at the confluence of water masses from the subarctic Pacific, via the California Current, and from the eastern tropical North Pacific, via the California Undercurrent, which interact with the local topography, coastline, and atmospheric forcing to sustain variability in circulation on inter-annual, seasonal, and intraseasonal time scales (Bograd et al., 2015; Dong et al., 2009). The effects of this variability in circulation has profound consequences for coastal ocean biogeochemistry (Gruber et al., 2011; Bograd et al., 2015; Nagai et al., 2015; Nezlin et al., 2018), and is therefore critical that the model accurately simulates spatial and temporal variability in circulation patterns.

Analysis of ocean circulation shows that the model successfully reproduces observed current patterns in the SCB. The dominant current in the coastal band of the SCB flows northward, and follows the topography along isobaths on the shelf. In the northern SCB, The model shows similar qualitative and quantitative patterns for the horizontal circulation

323   described in Dong et al., 2009. The intensity of the current is on average about 15 cm s^{-1}.
324   Vortices are generated inside the Santa Barbara Channel when the northward current that
325   flows along the Ventura coast meets the eastern side of Anacapa and Santa Cruz Islands,
326   with higher intensity in summer (Fig. 3). Submesoscale eddies are particular prominent
327   inside the Santa Barbara Channel. Persistent cyclonic eddies drive an upward doming of
328   isopycnals (McGillicuddy Jr, 2016), which supplies nutrients to the euphotic layer. The
329   model correctly reproduces this vertical transport, described in Brzezinski & Washburn,
330   2011, reproducing the high concentrations of nitrate and other nutrients in the upper layers
331   of the Santa Barbara Channel, in particular near the coast and around the Channel Islands,
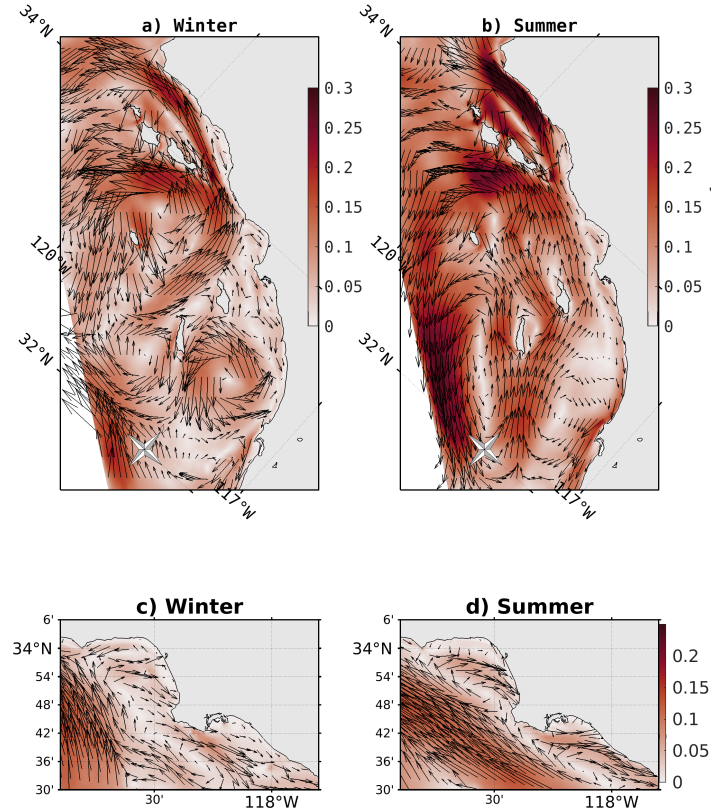332   as detailed in Section 4.3.1.

Figure 3: Mean modeled barotropic currents in the Southern California Bight. (a) Winter; (b) Summer; (c) Winter for the Santa Monica and San Pedro Bays; (d) Summer for the Santa Monica and San Pedro Bays. Arrows show the direction of the currents, and background colors the intensity. The strongest branch of the northward coastal current is located in the Santa Barbara Channel. Note the re-circulation in the Santa Monica and San Pedro Bays, intensified in summer.

333   In the central and southern SCB, the model successfully captures flow regimes around
334   the large POTW outfalls, indicating that it can appropriately represent the dispersal of
335   wastewater plumes in these regions. In the Santa Monica and San Pedro Bays, topography
336   drives the circulation of currents inside the Bays, converging back to the main current

offshore. On top of the Hyperion and JWPCP outfalls (respectively in the Santa Monica Bay and offshore of the Palos Verdes peninusula), the current is mostly south-eastward. In southern San Pedro proximal to the OCSD outfall, the current direction varies in winter between south-eastward and north-westward, but is primarily southward in summer. At the Point Loma outfall, the current is narrow, with a dominant south-eastern direction, parallel to the coast, as also shown by high frequency radar data (Terrill et al., 2006, https://www.sccoos.org/data/hfrnet/).

4.2 Vertical gradients and seasonal variability of temperature and the mixed layer depth

The model successfully reproduces the three-dimensional and seasonal variability of physical tracers, here exemplified by temperature. Temperature is the parameter in which we have the highest confidence in the observational record, because observations are abundant, and sensors are accurate and precise, regularly calibrated, and with negligible drifts. The greatest source of observational uncertainty is temporal under sampling and also to model biases (e.g. from atmospheric forcing, wind or shortwave detailed in Renault, McWilliams, et al., 2020). Quantitative statistical analysis indicates that model performance is '*excellent*' or '*very good*' for nearly all metrics for all regions and seasons (see Table 2). The lowest performance of the model is characterized as '*reasonable*' for the certain sub-regions (Palos Verdes, Orange County, and San Diego) in the spring and fall (Palos Verdes only) (see Supporting Information Table 2). As noted above, this may be due to under-sampling during these months, which can be highly variable because the region is shifting between a well-mixed to a more stratified ocean regime.
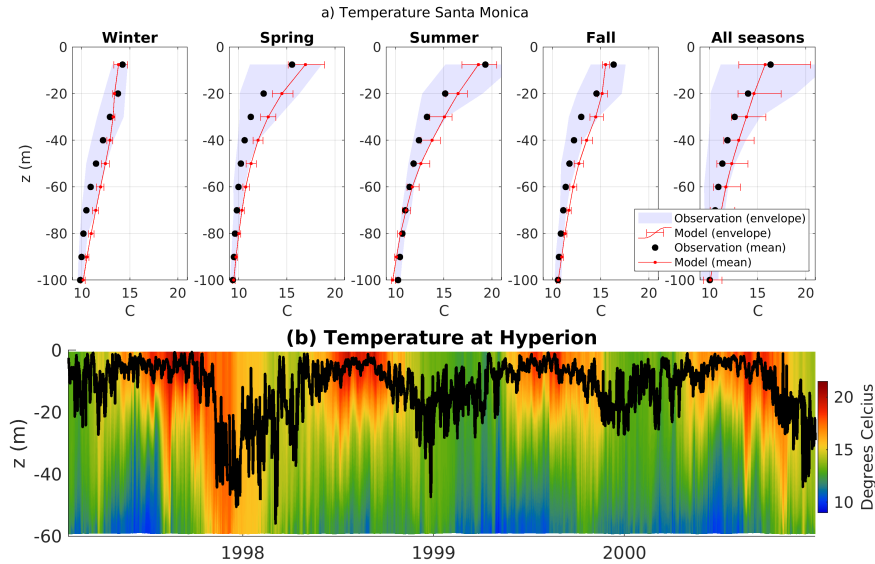

Figure 4: (a) Average seasonal profiles of temperature in the Santa Monica Bay. The red lines and red bars show the spatio-temporal mean and the variability from the model respectively. The black dots and the gray shading show the spatio-temporal mean and the variability from *in situ* data respectively. (b) Hovmöller diagram of temperature at the location of the Hyperion POTW outfall in the Santa Monica Bay. The black line shows the time-series of mixed layer depth. The deepest mixing occurs during El Niño 1998 (>40 m).

Following common practices (Montégut et al., 2007), we define the mixed layer depth (MLD) as the depth at which the temperature decrease from its surface value by more than 0.2 °C. On average, the MLD deepens from the coast to offshore, and varies with season. The model successfully simulates the seasonal cycle of MLD along the coast. For example, the model recreates seasonal deepening of the mixed layer in the Santa Monica Bay to greater than 25 m depth (the typical depth of the POTW plumes, see the Section 4.3.2) nearly every winter (black line in the Fig. 4b). The model also reproduces interannual variability in MLD under the influence of El Niño-Southern Oscillation (ENSO, hereafter referred to as El Niño) (e.g. the period from fall 1997 to spring 1998 in Fig. 4b). We show that during winter and spring of an El Niño year, the entire water column of the SCB is warmer than on average, and temperature is homogeneous, varying between 14 and 16 °C (Fig. 5e). Regular winter shows a homogeneous upper layer of < 13 °C temperature, and a mixed layer located at 40-60 m. The surface ocean is colder around the Channel Islands (SST<12 °C) (Fig. 5a). In summer, stratification is strongest, reflecting an intense vertical temperature gradient, and the MLD is found few meters below the surface (approximately 10 m). Temperature varies rapidly from more than 20 °C at the surface in the southern domain (16-17 °C in the northern domain) to less than 12 °C at 50m depth over the entire SCB (Fig. 5c). These patterns of variability in temperature are consistent with regional observations of El Niño in the SCB (Todd et al., 2011).

The model simulates the strong signature of upwelling in the northern SCB along the coasts of Ventura and Santa Barbara, consistent with observations (Bograd et al., 2015) (see Supporting Information: Fig. 31). The model shows a low-temperature upwelling signature with an average width of only a few kilometers, which manifests as multiple short and intense events during which relatively dense water ($\rho < 25.6$ kg m^{-3}) is injected into the mixed layer. In the central and southern domain, dense waters from upwelling rarely reach the surface, but drive a shoaling of the mixed layer along the coast, consistent with observations in this region (Seegers et al., 2015).
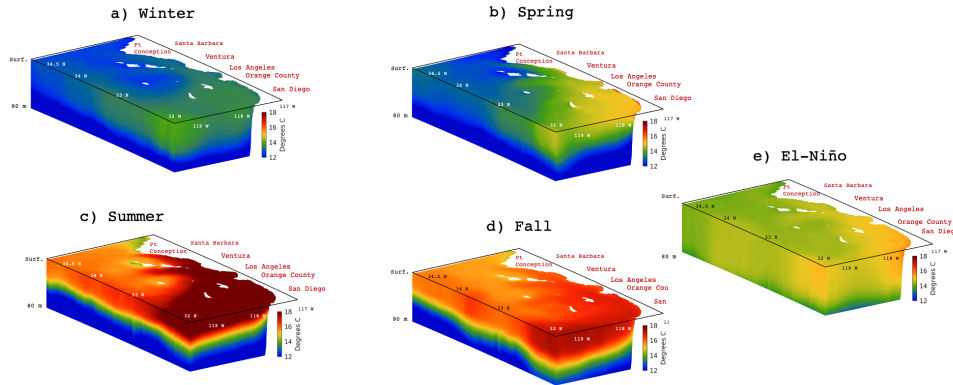

Figure 5: Three-dimensional illustration of the seasonality of temperature in the Southern California Bight. Panels (a-c) show winter, spring and summer respectively, while panel (d) shows an average for El Niño period (winter 1997 to the beginning of spring 1998).

	H	Correlation Coefficient	p-value	Cost Function	Percentage Bias	Ratio of Standard Deviations	Nash-Sutcliffe Model Efficiency	Number of observations
					Santa Monica: Temperature			
Winter	0	0.9588	1.21E-05	0.4038	-0.0429	1.0785	0.7869	716
Spring	0	0.9809	5.68E-07	0.5456	-0.0964	0.8022	0.5627	716
Summer	0	0.9607	9.94E-06	0.251	-0.039	0.9857	0.888	712
Fall	0	0.9364	6.63E-05	0.3857	-0.0462	0.9873	0.7781	718
All Seasons	0	0.9631	7.79E-06	0.338	-0.048	1.0013	0.8389	2862

Table 2: Statistical comparison between *in situ* data and model outputs for temperature profile in Santa Monica Bay.
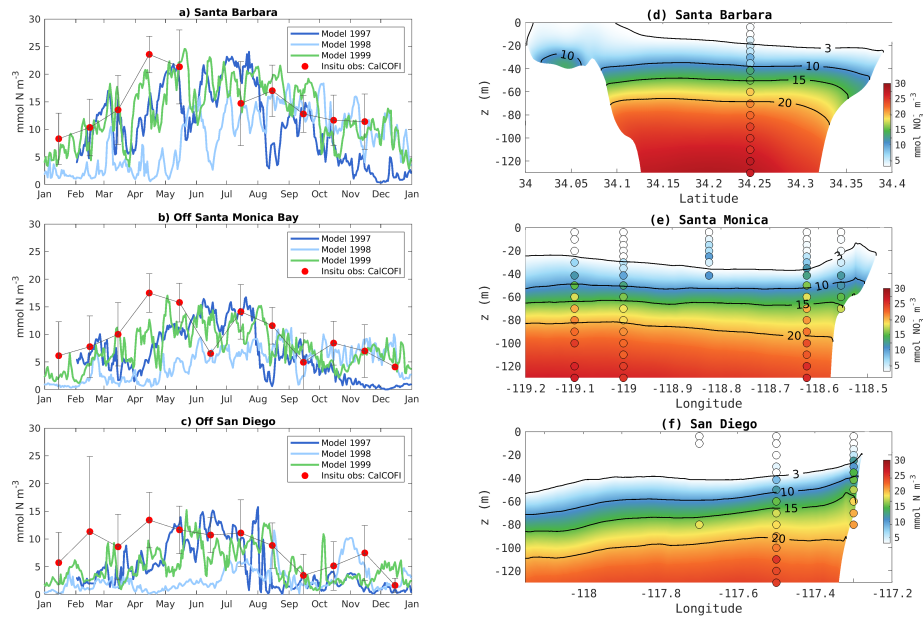

Figure 6: (a,c,e) Time series of nitrate concentration at 50m depth in three different locations of the SCB (a) SB: in the center of the Santa Barbara Channel; (c) SM: the coast off Santa Monica (e) SD: the coast off San Diego. Model outputs are represented by the lines for three different years, with the dots showing mean values from *in situ* measurement from CalCOFI, and gray bars the standard deviation from the mean. The time-series show prominent interannual variability in addition to seasonal variability. While the years 1997 and 1999 show similar nitrate distributions, the El Niño period between the end of 1997 to 1998 is significantly different, showing nearly uniform concentrations between November 1997 through May 1998. This is caused by the deepening of the thermocline during El Niño, which depresses the nutricline. (b,d,f) Cross sections showing the average springtime nitrate concentration in (b) the Santa Barbara region (d) the SM region, and (f) the SD region. Background are model outputs and dots are CalCOFI *in situ* measurements. Model and *in situ* data agree on the vertical and seasonal patterns in the three regions. They highlight the main differences in these three regimes, that reside in the shoaling of the nitraclines, closer to the surface in the Santa Barbara Channel and deeper in the southern waters.

4.3 Dissolved Inorganic Nitrogen

4.3.1 Spatial patterns and seasonality of nitrate

Nitrate observations are only available in the offshore CalCOFI dataset, so only broad regional patterns in nitrate concentration can be validated. There is a clear seasonality of nitrate, where surface concentrations are higher in spring and summer, and decrease in fall and winter (Fig. 6). The model reproduces the average seasonal patterns observed in the *in situ* nitrate data across multiple regions. The model also captures along-shore variability in coastal nitrate concentrations, reproducing values greater than 25 mmol N m^{-3} off Santa Barbara, 20 mmol N m^{-3} off Los Angeles, and 15 mmol N m^{-3} off San Diego.

The model also reproduces observed patterns in the depth of the nitracline (Mantyla et al., 2008; Nezlin et al., 2018), which tends to follow sloping density surfaces in the region. These patterns include: the high values at the euphotic depth ($\sim$50m below the surface) along the Santa Barbara coast in spring; the doming of the nitracline in the center of the Santa Barbara Channel 6b; the 20 to 30m deep nitracline along the Los Angeles coast; and the deepening of the nitracline from about 30 m at the coast to more than 60 m offshore in San Diego. In the offshore region of the SCB, the model is consistent with observations showing high nitrate ($>$20 mmol N $^{-3}$) around the Channel Islands (Fig. 6g) compared to less than 5 mmol N $^{-3}$ farther offshore. This pattern is strongest in winter and summer, when the offshore regions are particularly oligotrophic (surface NO_3^- $<$ 1 mmol m^{-3}) throughout the SCB.

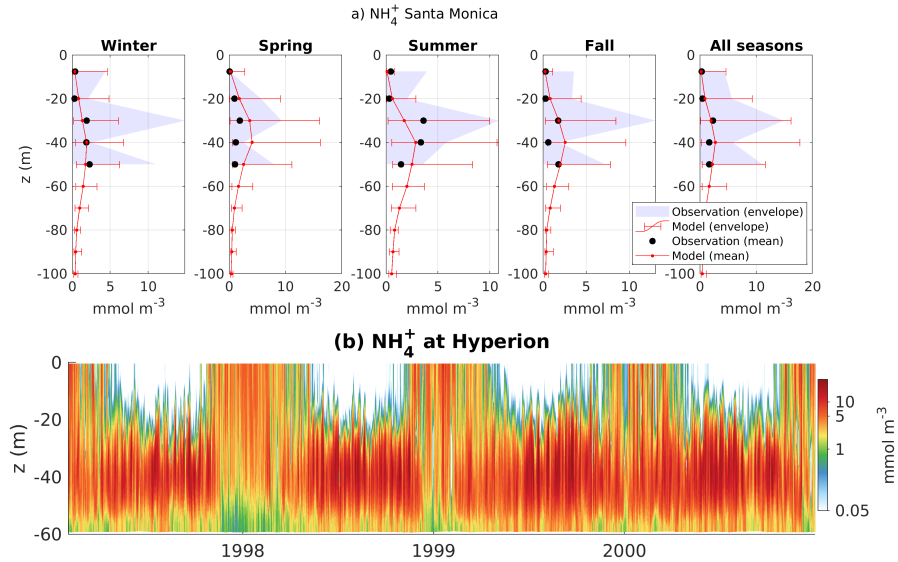#### *4.3.2 Vertical gradients and seasonal variability of ammonium*

Figure 7: As for Fig. 4, but for ammonium concentration. These profiles are showing agreement on intensity, seasonality and shape of the vertical profile with exceptionally high concentrations at mid-depth.

Ammonium concentrations above a natural background concentration of 1 mmol m-3 are indicative of POTW wastewater plumes. The model reproduces the observed average vertical profile of ammonium in Santa Monica Bay, falling within the range of observed vari-

Santa Monica: Ammonium							
	H	Correlation Coefficient	p-value	Cost Function	Percentage Bias	Ratio of Standard Deviations	Nash-Sutcliffe Model Efficiency	Number of observations
Winter	0	0.9202	0.0798	0.4071	0.1218	1.7604	0.7192	20
Spring	0	0.9324	0.0676	1.3485	-1.0256	0.562	-2.5435	21
Summer	0	0.6352	0.3648	0.5601	0.1716	1.7014	0.3634	21
Fall	0	0.9549	0.0451	0.2573	-0.1697	1.066	0.8527	21
All Seasons	0	0.8389	0.0757	0.5884	-0.2599	1.0185	0.387	83

Table 3: Statistical comparison between *in situ* data and model outputs for ammonium profile in Santa Monica Bay.

ability (Fig. 7a). Similar figures for other regions are shown in the Supporting Information, including Oxnard-Ventura (see Supporting Information: Fig. 26), Palos Verdes (see Supporting Information: Fig. 25, Orange County (see Supporting Information: Fig. 27) and San Diego. All regions show a similar maximum concentration between 30 to 45 m below the surface, in all seasons. The highest concentrations are seen in summer, when stratification is stronger, while lower concentrations in winter likely reflect increased dilution by seasonal mixing (Fig. 7b). Near ocean outfalls, both model and observations show mid-depth peaks of ammonium concentration, occasionally exceeding $10 \, \text{mmol m}^{-3}$, which considerably overshadow values observed away from outfalls. These high modeled ammonium concentrations are caused by wastewater plumes.

The main source of uncertainty in data-model comparisons is the lack of spatial and temporal coverage of measurements. Ammonium is typically measured near ocean outfalls and is therefore biased towards high concentrations, but the dataset is highly variable. Methodological difficulties exist with the measurement of ammonium in seawater, and as such, we excluded non-detectable ammonium values in our analyses. Near the subsurface outfalls, ammonium concentrations are likely extremely heterogeneous due to plume filaments, as observed in DiGiacomo, Washburn, Holt, & Jones, 2004 and in Warrick et al., 2007 in the Santa Monica Bay, as well as in other regions (e.g. Florida, Marmorino, Smith, Miller, & Bowles, 2010). Similarly heterogeneous plume dynamics are simulated in Minna Ho, n.d. with a very high resolution (dx<3 m) idealized model. As a result, the under sampling of ammonium may have led to poor statistical agreement between observations and model output (Table 3). The model shows high to moderate agreement for the shape of the profile and the mean concentration (Table 3). However, p-values for the correlations were not always significant (Table 3). Similarly, there were often biases and low performance regarding variability statistics. This low model performance can be explained by the following two reasons: (1) sampling is likely missing plume filaments, for example data points with high ammonium values likely capturing the plume are recorded next very low values; and (2) the resolution of the model (0.3 km), as well as model averaging over the day, season, and depth range causes plume filaments to appear more uniformly spread near the outfalls. Because plume filaments are lost in this averaging, the model represents plumes as cloud-like distributions around outfalls; nevertheless, the average ammonium concentration of wastewater plumes is reasonably well represented.

4.3.3 Horizontal gradients of ammonium

Both *in situ* observations (dots in Fig. 8, Fig. 7a) and model output (background colours in Fig. 8 and red line in Fig. 7a) show high concentrations of ammonium in the subsurface layer below the thermocline (Fig. 8c), which we refer to as "high-ammonium
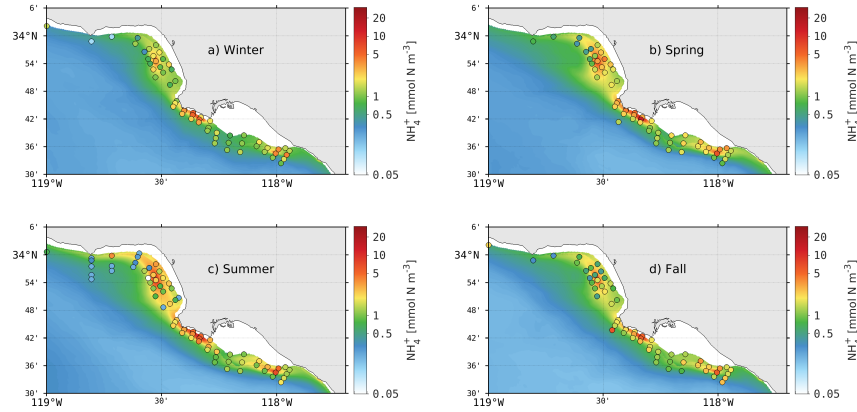
Figure 8: Colors show seasonal average ammonium concentration between 30 and 45m depth from the model, and dots from observations. High values highlight the spatial expansion of the subsurface wastewater plumes along the Orange and Los Angeles Counties. The highest concentrations are located within a narrow band of about 10-15km width, and are carried along the topography by the mean currents.

plume". This high-ammonium plume can extend from Huntington Beach to South Ventura, encompassing three of the four major wastewater treatment plant outfalls in the SCB (See Section 2.4). Both the model and observations show that the width and strength of the high-ammonium plume are greatest in summer compared to other seasons. The Santa Monica Bay Observatory (SMBO, Leinweber, Gruber, Frenzel, Friederich, & Chavez, 2009) located 17 km north-west of the submarine pipe Hyperion in Santa Monica Bay (Fig. 9a) frequently recorded concentrations higher than $2\,\mathrm{mmol\,m^{-3}}$, and up to $6\,\mathrm{mmol\,m^{-3}}$ at mid-depth, consistent with the model. The depth of the maximum variability is at 40 m in the model, and slightly shallower in the SMBO data, possibly because of a mismatch in the time period (1997-2000 for the model, and 2004-2010 for the SMBO). During winter, the model indicates vertical mixing and dilution of the plume at the surface. Accordingly, ammonium concentrations decrease slightly ad depth (Fig. 8a) and increase at the surface, reaching values up to $2\text{-}6\,\mathrm{mmol\,m^{-3}}$, also consistent with observations around the outfall pipes (Fig. 7a).

4.3.4 Spatial patterns in rates of nitrogen transformation

Although we had no *in situ* nitrogen transformation rates with which to compare model output during the simulation period, several datasets exist for the region that can serve as a test for whether the model is simulating reasonable patterns in rates via the right mechanisms. We found that modeled rates do agree with observed nitrogen transformation rates. Nitrification rates, the sequential oxidation of NH_4^+ to NO_3^- via NO_2^-, have been observed to be higher within wastewater plumes in the SCB a pattern driven by high ammonium concentrations in the discharges (McLaughlin, Nezlin, et al., 2017). In both observations and the model, nitrification predominately occurs below the euphotic layer. Modeled vertically-integrated nitrification rates vary between 0.15 and $1.5\,\mathrm{mmol\,N\,m^{-2}d^{-1}}$, consistent with observations within the SCB and in the California Current (Table 5). The model also reproduces the spatial pattern of higher rates within wastewater plumes (Supporting Information Fig. 32). There is also good agreement between observed and modeled rates of nitrate and ammonium uptake by phytoplankton communities and (Kudela et al., 2017). Modeled nitrate uptake rates vary between 2 and $11\,\mathrm{mmol\,N\,m^{-2}d^{-1}}$ and ammonium uptake rates
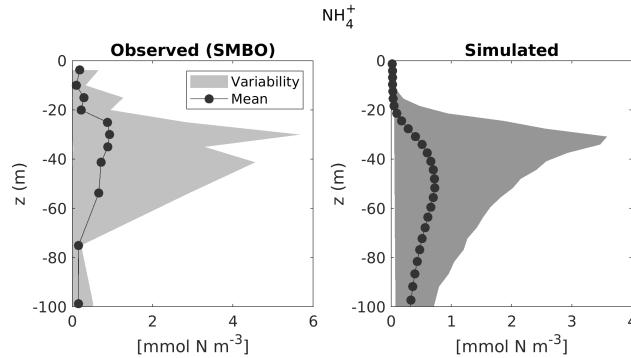
−17−

Figure 9: Statistical comparison of the vertical profile of ammonium at SMBO. It informs that the plume signature in ammonium concentration is apparent 17 km far from Hyperion outfall.

vary between 6 and 51 mmol N m^{-2}d^{-1} in the Los Angeles and Orange County coasts, consistent with observations in the SCB (Table 5).

4.4 Chlorophyll concentrations

In general, the model was found to reproduce vertical and horizontal gradients in chlorophyll (a proxy for phytoplankton biomass) in different subregions (Fig. 12). The timing of blooms was consistent with changes in mixing and nutrient delivery in the SCB. We present three different subregions characterized with distinct hydrodynamic regimes: the Santa Barbara Channel, and the Los Angeles and San Diego coasts.

There are several sources of uncertainty in the chlorophyll, primary production, phytoplankton growth, and grazing rates observational records. For chlorophyll, bottle measurements are accurate and precise, but measure a limited portion of the water column. Sensors are accurate and precise in their measurement of fluorescence and have a rapid response time, providing vertically resolved profiles; however, the algorithm to convert fluorescence to chlorophyll concentration is inaccurate for the SCB. As a result, a correction factor has been applied to Bight data which adds uncertainty to the observational dataset (Nezlin et al., 2018). Satellite measurements of chlorophyll are inferred from ocean color (Kahru et al., 2009). This method works well offshore, but breaks down nearshore where terrestrially-derived colored dissolved organic matter creates uncertainty in reported satellite chlorophyll estimates on the order of 100% or greater (Zheng & DiGiacomo, 2017). For primary production, the incubation method to derive the rates is sensitive and precise (Cullen, 2001), though measured rates are subject to bottle effects and there is some ambiguity as to whether the experiments measure net primary production or gross primary production (Regaudie-de Gioux et al., 2014). Phytoplankton growth and zooplankton grazing are also determined experimentally, and duplicate measurements indicate that these methods are not very precise, with differences between duplicates ranging from 80% to 200% (Landry et al., 2009; Li et al., 2011). For all three measurements, spatial and temporal under-sampling, particularly during seasons with high variability, adds uncertainty to the data-model comparison.

4.4.1 Horizontal gradients in chlorophyll

Despite the uncertainties outlined above, the model successfully simulates horizontal gradients in chlorophyll in the three subregions (Santa Barbara, Los Angeles and San Diego). The model captures the early, wide-spread spring bloom in the Santa Barbara Channel,

which occurs as a combination of a coastal bloom driven by spring upwelling, followed by a bloom in the central and southwestern regions of the Channel (near the islands) in spring and summer (Fig. 10). The latter is driven by the strengthening of the cyclonic circulation in the Channel, which transports nutrients to the upper layers, and is regularly observed in the region (Brzezinski & Washburn, 2011). The model captures the strong seasonality in chlorophyll, wherein concentrations change from near zero in winter to up to $8\,\mathrm{mg}\,\mathrm{Chl}\,\mathrm{m}^{-3}$ in spring. Of the three regions, the blooms off Santa Barbara extends into late summer and fall, where the average concentration is approximately $1\text{-}2\,\mathrm{mg}\,\mathrm{Chl}\,\mathrm{m}^{-3}$, a pattern replicated in both model and observations .
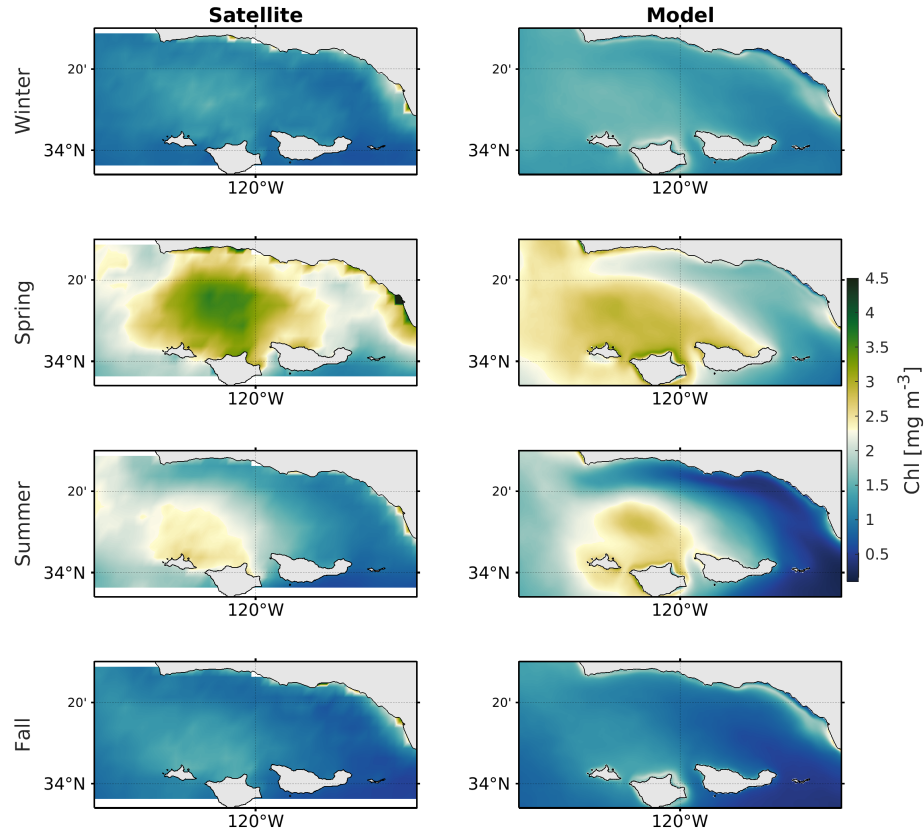

Figure 10: Comparison of seasonally-averaged surface chlorophyll between SeaWiFS remote sensing data (left panels) and the model (right panels) in the Santa Barbara Channel, where an important seasonal bloom is observed.

In the Los Angeles subregion, the model predicts broad patterns in chlorophyll concentrations, including a persistent bloom in the San Pedro Bay, consistent with observations (Nezlin et al., 2012), and validated by comparison with remote sensing (Fig. 11). Both satellite and modeled data show concentrations in the San Pedro Bay consistently higher

than 3 mg Chl m^{-3} year-round, often extending into the Santa Monica Bay. The model also reproduces the strong offshore gradients in chlorophyll, where across less than 15 km offshore surface concentrations are reduced 3 to 4 fold ($<$1 mg Chl m^{-3}) further decreasing offshore. The model also reproduces the timing and magnitude of the blooms in the Santa Monica and San Pedro Bays. The difference in timing of maximum chlorophyll concentrations between the Santa Monica and San Pedro Bays likely reflects differences in nutrient supply. Nutrients, in particular ammonium, are available near the surface during winter (see Section 4.3.2), reflecting more vigorous mixing of the wastewater plume and land-based nutrient supply by rivers (in particular in the San Pedro Bay) during winter storms (Lyon & Stein, 2009). Storms and winter mixing events have been connected to phytoplankton blooms in the region (Nezlin et al., 2012; Mantyla et al., 2008). Further offshore in the Los Angeles region, the model recreates the weak seasonality of surface chlorophyll, with higher concentrations during winter and spring, and lower concentrations in summer and fall. In the offshore region of Santa Monica Bay, the seasonal cycle is marked by the increase of surface phytoplankton between March and May as shown in Fig. 12b. Mean chlorophyll values reach up to 3 to 4 mg Chl m^{-3} in April and May, although concentrations below 2 mg Chl m^{-3} are more common, consistent with observations over the same period.

Offshore of the San Diego coast subregion, the model recreates a slight increase in surface chlorophyll in March; however, concentrations are generally below 1 mg Chl m^{-3} year-round (Fig 12c). The oligotrophic conditions of the southern Bight (Nezlin et al., 2012; Mantyla et al., 2008) have been attributed to a deeper nitracline, which in turns supports a deep chlorophyll maximum layer (Mantyla et al., 2008). This feature is well represented in the model, which reproduces relatively high concentrations of chlorophyll in subsurface layers (generally between 20 and 90 m depth) in the region (Fig. 14b-c).

4.4.2 Vertical gradients and seasonal variability of chlorophyll

The goodness-of-fit statistical metrics (correlation coefficient and cost function) for chlorophyll are generally *excellent* or *very good* for most seasons for all sub-regions (see Table 4). We were most concerned with performance for these metrics because the remaining statistics may be affected by the aforementioned uncertainties due to the fluorometry calibration. The observational measurements should be internally consistent (if not accurate), so the shapes of profiles should be "correct" even if the magnitude is off due to poor calibration, and the model was able to replicate these shapes accurately. Despite calibration issues, the model reproduced chlorophyll reasonably well for the northern Bight sub-regions: Santa Monica Bay (Fig. 13), Palos Verdes (Supporting Information: Fig. 28), and Ventura/Oxnard (see SI, Fig. 29), reproducing the magnitude and general shape of observed profiles. However, the model did not capture the variability for most regions (except for Palos Verdes), generally scoring *reasonable* or *poor* in the ratio of standard deviations for most seasons, particularly spring. This is likely a result of the spatial and temporal averaging. Chlorophyll is highly variable in space and time and under-sampling in either of these dimensions will adversely affect variability estimates for a region and season. Therefore, reasonable performance for these metrics was not unexpected.

Model performance was lowest in the southern Bight regions, San Diego and Orange County (see Supporting Information: Fig. 30). Model predictions in San Diego consistently underestimate chlorophyll concentrations, a result likely driven by the fact that Mexican cross border wastewater inputs are not included in this simulation. Similarly, underestimation of chlorophyll along the Orange County coast could be linked to the underestimated nitrate in OCSD's wastewater effluent data. Despite the poor performance scores for some of the metrics related to the underestimation of chlorophyll, the correlation and goodness of fit metrics are generally excellent or very good for these two subregions. This suggests that the model may provide a conservative estimate of phytoplankton biomass in the southern Bight, while reproducing accurate spatial and temporal patterns in that biomass.
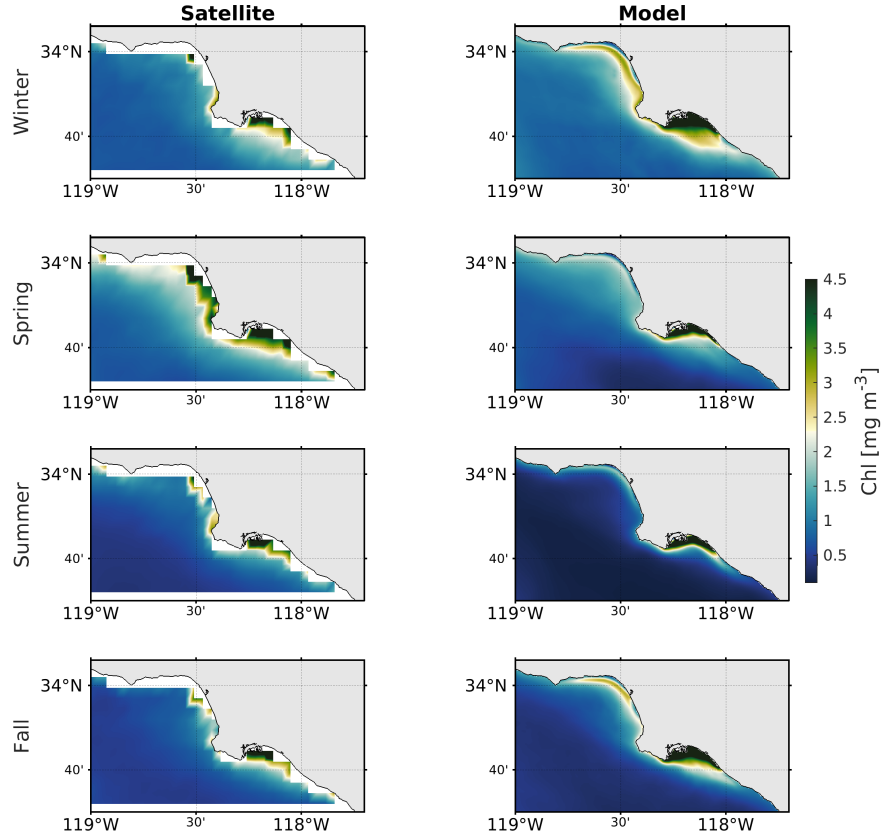
Figure 11: Comparison of seasonally-averaged surface chlorophyll between SeaWiFS remote sensing data (left panels) and the model (right panels) for years 1998-2000 in the Santa Monica and San Pedro Bays, where major POTW outfalls are found. The figure highlights the persistent coastal phytoplankton bloom, and the sharp inshore-offshore gradients.
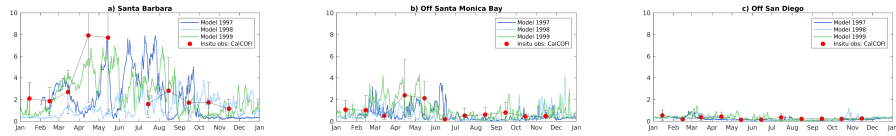

Figure 12: Comparison of surface chlorophyll concentration between different years of model output, and a climatology from CalCOFI *in situ* data. SB is near the center of Santa Barbara Channel, SM is offshore the Santa Monica Bay, and SD is offshore San Diego. The model reproduces different productivity regimes across the Southern California Bight, with highly productive waters in the northern region, where average concentrations greater than $3\,\mathrm{mg\ m^{-3}}$ are observed for more than half of the year, and oligotrophic southern regions, where average surface concentrations rarely exceed $1\,\mathrm{mg\ m^{-3}}$.

In addition to transporting nutrients from depth, upwelling 'seeds' surface waters with subsurface water masses dominated by selected phytoplankton species, stimulating surface blooms near the coast (Seegers et al., 2015). The model successfully reproduces this process, wherein the subsurface chlorophyll maximum shoals and intensifies in spring, forced by the vertical movement of the thermocline driven by upwelling. This seasonal dynamics occurs across the domain in the model.

Offshore, in the more oligotrophic portion of the SCB, the model predicts that more than 60% of the maximum concentration of phytoplankton biomass remains below the surface all year (see Supporting Information: Fig. 33), constantly fed by subsurface nutrients injections. This is consistent with observations of a deep chlorophyll maximum throughout the region (Nezlin et al., 2018; Mantyla et al., 2008; Seegers et al., 2015), and to observations at the San Pedro Oceanic Time-Series, SPOT, located between the Palos Verdes Peninsula and Catalina Island. At SPOT, a region weakly influenced by anthropogenic nutrients inputs at the surface, the model realistically simulates the seasonal cycle of chlorophyll. While ammonium does not exceed typical "natural" values of $\sim$1 mmol m^{-3} below the surface (see Supporting Information: Fig. 33), chlorophyll concentrations regularly reach more than 2 mg m^{-3} between 20 and 40 m in summer (see Supporting Information: Fig. 33), in agreement with *in situ* measurement (Teel et al., 2018; Beman et al., 2011). However, in regions more heavily influenced by anthropogenic nutrients, such as the Santa Monica Bay, the chlorophyll maximum progressively deepens from the surface in winter to about 25 to 30 m depth in spring and summer, with chlorophyll concentrations exceeding 5 mg Chl m^{-3} (Fig. 13a). This subsurface chlorophyll maximum is maintained for four to five months (Fig. 13b) before the stratification is weakened by fall and winter mixing.
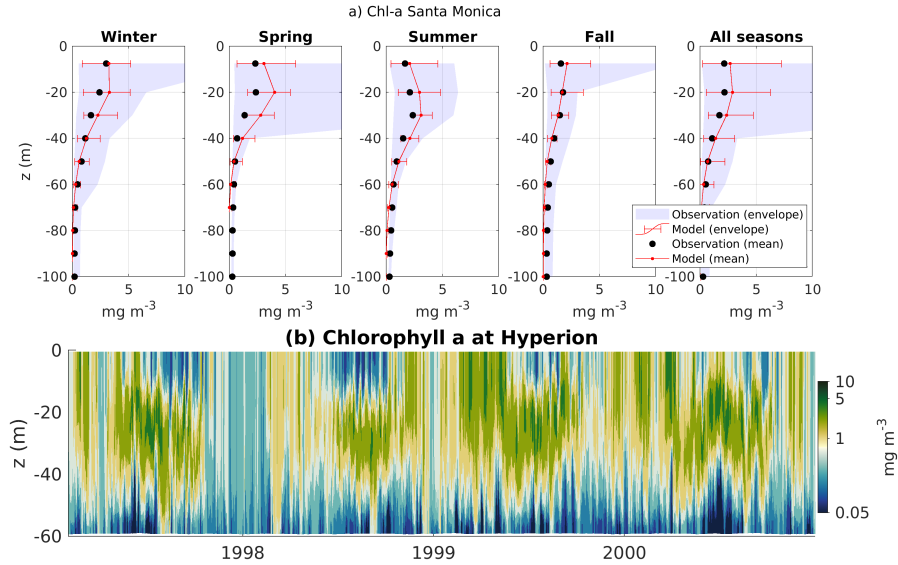

Figure 13: As for Fig. 4, but for chlorophyll concentration. Vertical profiles show a good agreement between simulated and *in situ* data, and display the formation of a subsurface chlorophyll maximum in summer, and a surface maximum in winter and spring. Concentrations in winter vary up to +5 mg Chl m^{-3}. Note the very low concentrations during 1998 El Niño in the entire water column.

Santa Monica: chlorophyll								
	H	Correlation Coefficient	p-value	Cost Function	Percentage Bias	Ratio of Standard Deviations	Nash-Sutcliffe Model Efficiency	Number of observations
Winter	0	0.985	2.19E-07	0.2925	-0.0661	0.7821	0.847	714
Spring	0	0.9729	2.28E-06	0.8293	-0.3853	0.5196	-0.3395	716
Summer	0	0.9958	1.40E-09	0.4615	-0.0558	0.6637	0.699	712
Fall	0	0.97	3.44E-06	0.5047	0.2114	0.7569	0.6708	718
All Seasons	0	0.9968	4.82E-10	0.4606	-0.0805	0.671	0.6932	2860

Table 4: Statistical comparison between *in situ* data and model outputs for chlorophyll profile in Santa Monica Bay.
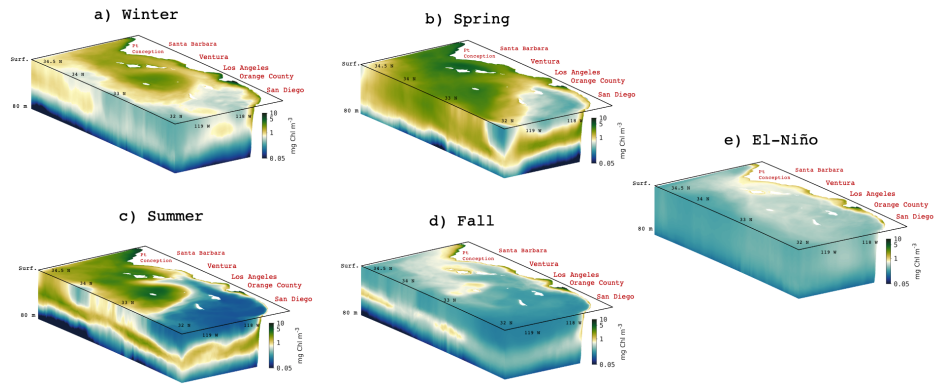

Figure 14: As for Fig. 5 but for the total chlorophyll concentration.
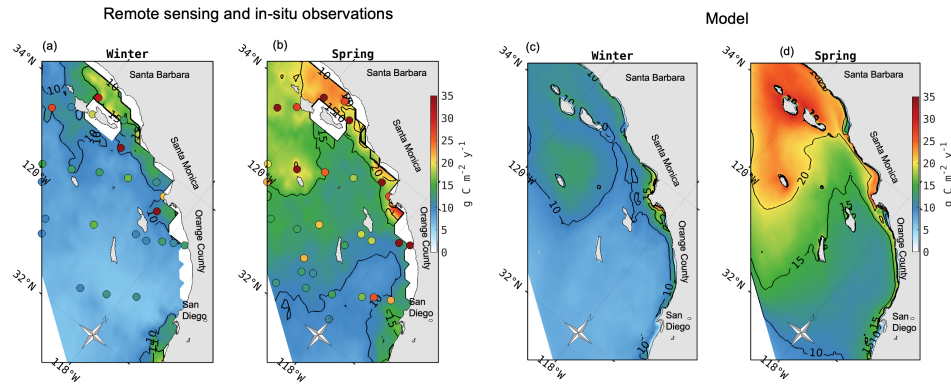

Figure 15: (a-b) Vertically integrated primary production from remote sensing algorithm (VGPM) and CalCOFI *in situ* measurements for winter (January and February) (a) and spring (April to June) (b). (c-d) Vertically integrated primary production from the model, in winter (c) and spring (d). Note the higher values for CalCOFI *in situ* measurements as compared to the satellite estimate, in better agreement with the model.

4.4.3 Primary production

Validation on rates of primary production, phytoplankton growth and zooplankton grazing (Table 5) provides an independent check on mechanisms responsible for chlorophyll as a state variable. The spatial and temporal frequency of these data, garnered from CalCOFI observations and literature values, is low. The most data as well as the most standardized methodologies are available for primary production (PP). However, many of the primary production measurements used in this validation do not temporally coincide with the model period. Despite these uncertainties, the model generally reproduces expected large-scale patterns and seasonal variability in primary production. This large scale variability was also mentioned in Deutsch et al., 2020. Model and data both show lower productivity in winter (Fig. 15a,c) and higher in spring (Fig. 15b,d), when the PP is high along the coastal band, in the northern Bight around the Channel Islands (Fig. 15d), consistent with observations (Fig. 15b). This is consistent with the "green ribbon" of high-chlorophyll observed along the coast throughout the SCB (Lucas et al., 2011). The model reasonably reproduces the seasonal cycle of PP in each of the subregions.

Phytoplankton are generally limited by a combination of nutrients and light, the latter of which is only limiting at depth in the SCB. In winter, nitrogen is high at the surface in the northern SCB, and thus is not limiting. In the southern SCB, light an nitrogen are co-limiting due to stronger stratification, leading to oligotrophic conditions. In spring and through the summer, nitrogen is limiting nearly everywhere except in the Santa Barbara Channel and near the Channel Islands, where upwelling and submesoscale eddies maintain high nutrients at the surface.

Finally, while slightly outside our model domain and simulation period, the modeled phytoplankton growth and zooplankton grazing rates were within the same order of magnitude as the measured rates from the California Current Long Term Ecological Research project (CC-LTER, see Landry et al., 2009) (Table 5) in the northern portion of the Bight.

	Bight 13	Literature	Model
Primary production (g C m^{-2} y^{-1})	47.4, 374.6, 1037.4		250, 1660
Nitrification (mmol m^{-3} d^{-1})	0, 0.03, 0.225	0.02, 0.04, 0.08	0.15, 1.5
NO$_3^-$ Uptake Rate (mmol N mg Chl^{-1} d^{-1})	0.005, 0.28, 2.16		0.03, 0.15
NH$_4^+$ Uptake Rate (mmol N mg Chl^{-1} d^{-1})	0.10, 1.33, 8.30		0.08, 0.15
Total Phytoplankton Growth μ (d^{-1})		0.05, 0.33, 0.8	0.3, 0.4
Grazing (d^{-1})		0.5, 0.26, 0.02,	1.5, 0.3

Table 5: Comparison of biogeochemical rates between literature and model. Model rates are derived from monthly climatologies.

4.5 Carbonate system and oxygen parameters

The model predicts changes in dissolved oxygen and carbon-system parameters related to photosynthesis and respiration processes, as well as horizontal transport and vertical mixing. As described in section 4.4.1, the coasts of Los Angeles and Santa Barbara are hotspots of intensified plankton activity, and both systems are impacted by high variability and small-scale eddy circulation. In the upper layers, photosynthesis increases both dissolved oxygen and pH (Figs. 17 and 20), consistent with observations in these regions. The Santa Monica Bay shows the highest oxygen production rates (60 mmol m^{-2} d^{-1}), followed by the Santa Barbara coast (57 mmol m^{-2} d^{-1}), while rates in the Orange County and San Diego coasts are nearly two times lower. Oxygen and carbon are further replenished at the surface

by air-sea gas exchange with the atmosphere. Export of newly-fixed organic carbon leads in both regions to high remineralization rates that consume oxygen and release carbon dioxide at depth. We simulate similar high organic matter export (around 30 mmol m^{-2} d^{-1}) in both the Santa Barbara and Los Angeles coasts (see Supporting Information: Fig. 34).

The reliability of these predictions can be tested through validation of dissolved oxygen and carbonate system parameters. There are several sources of uncertainty in the dissolved oxygen, pH, and aragonite saturation state observational records which affect data-model comparisons. For dissolved oxygen, sensors are relatively accurate and precise and have a rapid response time ($<$ 1s) creating vertically resolved profiles. Repeated field measurement accuracy for CTD dissolved oxygen sensors was reported to be approximately 8 mmol m^{-3} (Coppola et al., 2013). The pH observational record is particularly fraught with uncertainty. An evaluation of pH sensor data in the SCB indicated that, while sensor pH measurements were well correlated with discrete bottle samples collected at the same depth, there was a clear bias in pH, with sensor measurements under-predicting bottle measurements and high variability in the differences between paired bottle and sensor measurements (ΔpH ranging from +/- 0.5) (McLaughlin, Dickson, et al., 2017). The aragonite saturation state is estimated using an algorithm developed for the region (Juranek et al., 2011) for both *in situ* observations and model output, because complete measurements of carbon-system parameters required to calculate Ω_{Ar} are missing. For all three variables, spatial and temporal under-sampling, particularly during seasons with high variability, adds uncertainty to the data-model comparison.

4.5.1 Vertical gradients and seasonal variability of dissolved oxygen

The model reproduces observed seasonal and spatial patterns in dissolved oxygen concentration (Fig. 19), accurately simulating magnitude, vertical and horizontal gradients, and variability. Quantitative statistical analysis (see Table 6) indicated that the model performance was '*excellent'* or '*very good'* for nearly all metrics for all regions and seasons. The lowest performance of the model was characterized as '*poor'* for two sub-regions for the Nash-Sutcliff Model Efficiency during Spring, and '*reasonable'* for some metrics in some sub-regions, which may be related to under sampling during seasons with high variability, as described above. Similar to temperature, we tested whether the variability in spring may be impacting the performance statistics by extracting random profiles for the region (shown as green lines in the spring season plots in Fig. 17), which show how dissolved oxygen on a random single day can more closely align with the observations. This supports the hypothesis that observational uncertainty is behind the lack of observational agreement with the model. Model performance was lowest in the Orange County and San Diego sub-regions, where model predictions tended to overestimate dissolved oxygen, consistent with the chlorophyll underprediction, a likely consequence of the lack of cross-border inputs from Mexican waters.

The model also reproduces the seasonality in dissolved oxygen in all subregions (Fig. 17), characterized by large meridional and vertical variability. Near the Channel Islands, dissolved oxygen varies at 50 m by up to 140 mmol O$_2$ m^{-3} between the highest winter values and the lowest summer values, reflecting the dynamics of upwelling, productivity, and gas-exchange with the atmosphere. Offshore the Santa Monica and San Diego coasts, the variability between winter and summer is of the order of 80-90 mmol O$_2$ m^{-3}. Surface concentrations are everywhere above 240 mmol O$_2$ m^{-3} year-round, consistent with observations. The highest summer concentrations are observed at the depth of the deep chlorophyll maximum (Figs. 18c and 14), reflecting photosynthesis, while decreasing at depth to below 150 mmol O$_2$ m^{-3}. These patterns are generally consistent with observations in the same regions.

During the 1998 El Niño event, the model shows a net decrease of dissolved oxygen near the surface, and a net increase below it. During this period, the entire upper layer

680 (0-80 m) is characterized by a homogeneous concentration of about 240 mmol O_2 m^{-3} over
681 almost the entire SCB (Fig. 18e). Only the San Pedro and Santa Monica Bays show
682 higher concentrations, which we attribute to the local anthropogenic nutrient enrichment
683 and subsequent blooms (see Fig. 14e). This is consistent with observations of the 1998 event
684 in California coastal waters (Chavez et al., 2002; Booth et al., 2014).
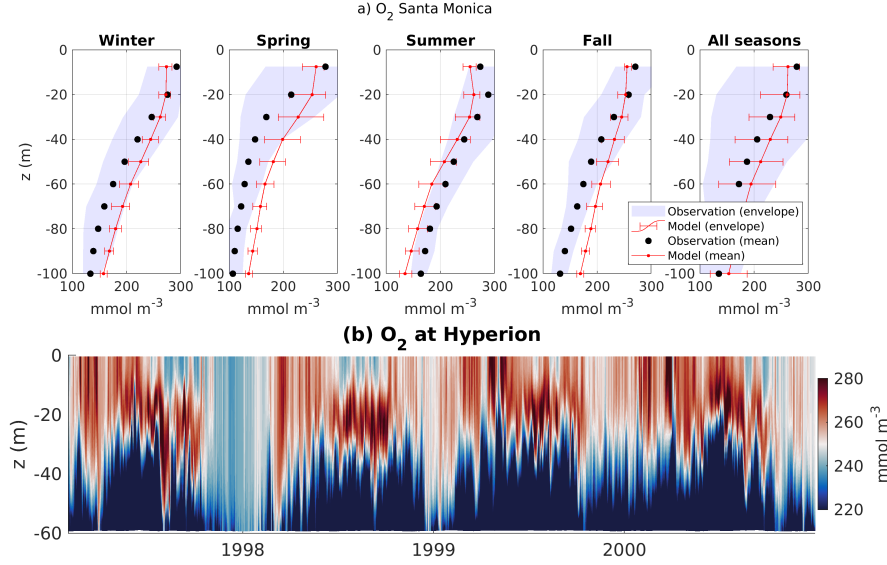

Figure 16: As for Fig. 4, but for oxygen concentration.

4.5.2 *Vertical gradients and seasonal variability of carbon-system parameters*

687 Together with pH, the saturation state of aragonite (Ω_{Ar}) is often used as a metric
688 to identify the potential impact of Ocean Acidification on marine calcifiers, because it is a
689 measure of the availability of carbonate ions for calcium carbonate precipitation (Bednarsek
690 et al., 2019). Ω_{Ar} shows similar vertical variability as dissolved oxygen (Juranek et al., 2009;
691 Alin et al., 2012). Similar to deoxygenation, reduction in pH and Ω_{Ar} in the upper layers is
692 generally caused by coastal upwelling or by local physical processes (Feely et al., 2018). We
693 utilize sensor pH data sets to evaluate vertical profiles in the carbonate system. Because of
694 the known uncertainty in pH measurements, we are most concerned with how well the model
695 reproduced the shape of the profiles (i.e., goodness of fit estimates, as with chlorophyll).
696 Sensor-derived pH profile measurements should be internally consistent within a data set
697 (if the sensor is working properly and if pressure issues are minimal), providing some value
698 to goodness of fit assessments. Given these constraints, the data-model comparisons for
699 pH sensor data were generally '*excellent*' or '*very good*' for all sub-regions and all seasons.
700 Unsurprisingly, the model performance reproducing observational means and variability
701 was generally '*reasonable*' or '*poor*' for most sub-regions and seasons, with some, if not
702 most, of this disagreement due to measurement error. Recently, the CalCOFI program has
703 incorporated Ω_{Ar} into its sampling program. Although the data do not line up with the
704 model period, they are useful for evaluating seasonal variability in the model . Generally,
705 the model reproduces seasonal and vertical variability in Ω_{Ar}, with higher saturation states
706 in the summer and fall, when waters are generally more stratified, and lower values in
707 winter and spring, when upwelling brings undersaturated waters closer to the surface. Ω_{Ar}
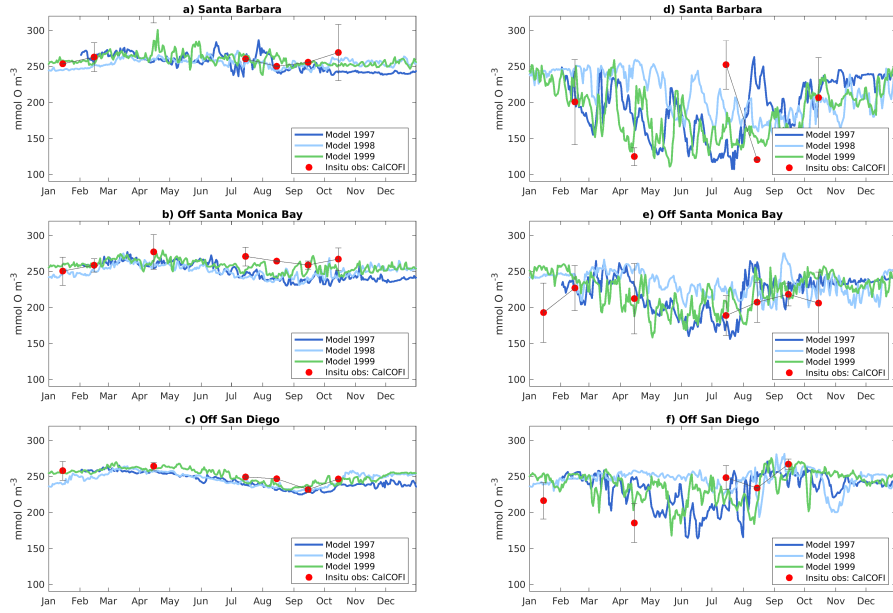
Figure 17: Comparison of dissolved oxygen concentration between different years of model output, and a climatology from CalCOFI *in situ* data. SB is near the center of Santa Barbara Channel, SM is offshore the Santa Monica Bay, and SD is offshore San Diego. Left panels show surface concentrations, right panels concentrations at 50 m depth.

	H	Correlation Coefficient	p-value	Cost Function	Percentage Bias	Ratio of Standard Deviations	Nash-Sutcliffe Model Efficiency	Number of observations
					Santa Monica			
					Oxygen			
Winter	0	0.979	8.35E-07	0.42	-0.1001	1.1802	0.7766	716
Spring	0	0.9297	9.80E-05	0.671	-0.2214	1.0738	0.4364	702
Summer	0	0.995	2.77E-09	0.32	0.065	0.9764	0.8686	712
Fall	0	0.9823	4.16E-07	0.548	-0.1175	1.3376	0.6115	718
All Seasons	0	0.9781	9.82E-07	0.3886	-0.0848	1.1058	0.8135	2848
					pH			
	H	Correlation Coefficient	p-value	Cost Function	Percentage Bias	Ratio of Standard Deviations	Nash-Sutcliffe Model Efficiency	Number of observations
Winter	0	0.9928	1.19E-08	0.515	0.0033	0.574	0.4817	632
Spring	0	0.9851	2.14E-07	0.8008	-0.0148	1.496	0.1897	702
Summer	0	0.9535	1.94E-05	0.2564	0.0026	1.0253	0.8466	712
Fall	0	0.9787	8.71E-07	0.2615	0.0029	1.3727	0.7886	715
All Seasons	0	0.9743	1.86E-06	0.2557	-0.0016	1.0741	0.9139	2761

Table 6: Statistical comparison between *in situ* data and model outputs for dissolved oxygen and pH profile in Santa Monica Bay.
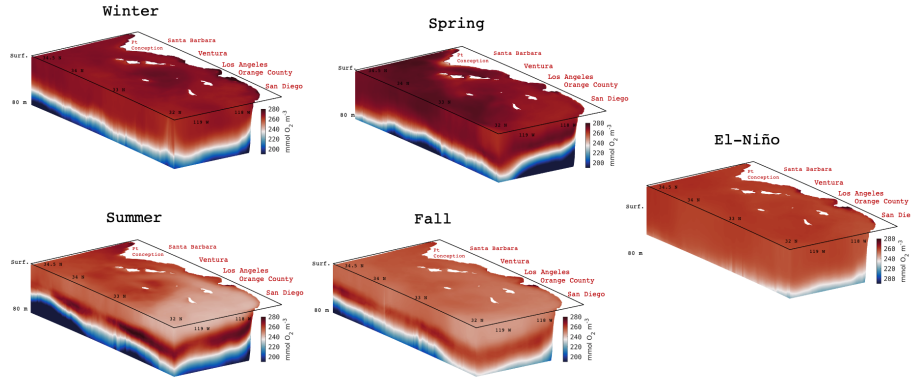
Figure 18: As for Fig. 5 but for dissolved oxygen concentration.

is also much lower and more highly variable at depth . These patterns are consistent with observations throughout the SCB (McLaughlin et al., 2018).

5 Summary

In this study, we demonstrated the readiness of high-resolution, dynamically down-scaled, physical-biogeochemical model to mechanistically investigate links between a comprehensive reconstruction of terrestrial and atmospheric nutrient inputs, coastal eutrophication, and biogeochemical change in the SCB coastal waters. This modeling plate-form is an important achievement because it strikes a balance of capturing the forcing of coast-wide basin mesoscale phenomena, while capturing the combined effects of bathymetry and submesoscale eddies that intensify transport of nutrients and biological material. Moreover, this model allows to run hindcast simulation of primary production, ocean acidification and deoxygenation at timescales that can approach the multi-decadal frequencies of intrinsic ocean variability, making the grand challenge of disentangling natural variability, climate change, and local anthropogenic forcing a tractable task in the near-term.

ROMS has a long history of validation and management acceptance through various applications in the CCS (e.g. Shchepetkin & McWilliams, 2011). In contrast, experience with BEC within the SCB is more limited. Our validation study of coastal eutrophication gradients in the SCB nearshore complements the U.S. West Coast-wide study of (Deutsch et al., 2020) and strengthens confidence that the basic CCS BEC model formulation, forcing and parameterization is appropriate not only for coastwide analyses but also for detailed local studies of coastal eutrophication in the highly urbanized SCB. The representation of physical processes such as vertical mixing and horizontal circulation was consistent across the model and measurements. The model reproduces the main structure of the climatological upwelling front and cross-shore isopycnal slopes, the mean current patterns and associated temperature gradients. We also demonstrate good agreement between model simulations and the mean distributions and variability of key ecosystem metrics, including surface nutrients and productivity, and subsurface O_2 and carbonate saturation. The spatial patterns of PP, phytoplankton growth rates, and zooplankton grazing are broadly consistent with measured rates. The distribution of PP is governed by the trade-off between nutrient and light limitation, a balance that reproduces and explains the observed spatial variations in the depth of the deep chlorophyll maximum. Statistical measures of model agreement on biogeochemical state variables was excellent to good and the range of predicted biogeochemical rates on par with observations. Under the realistic flow fields produced by ROMS, the
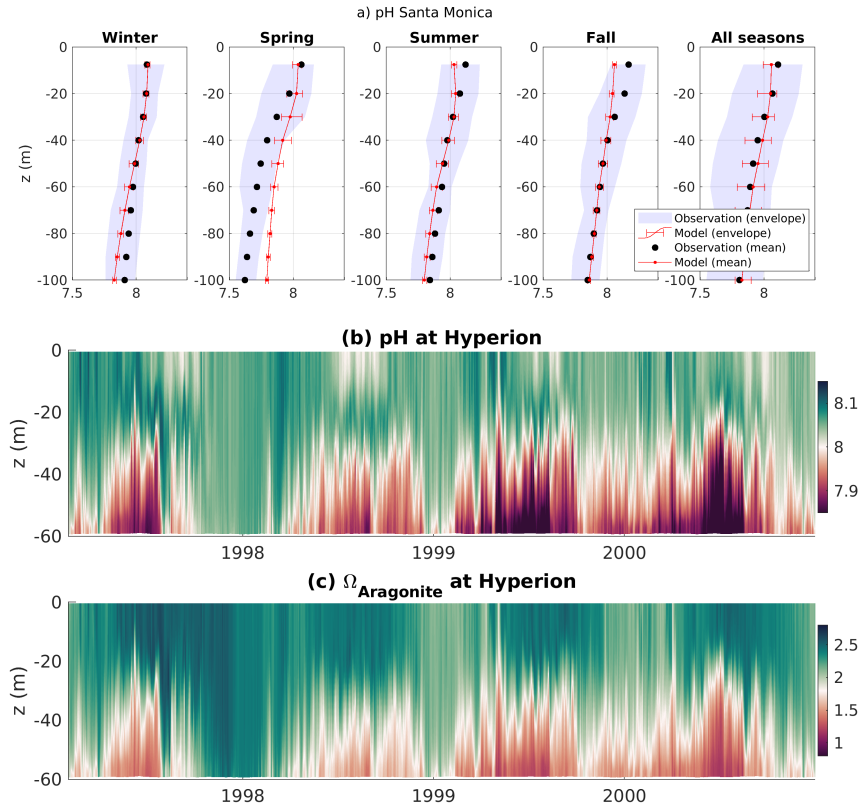
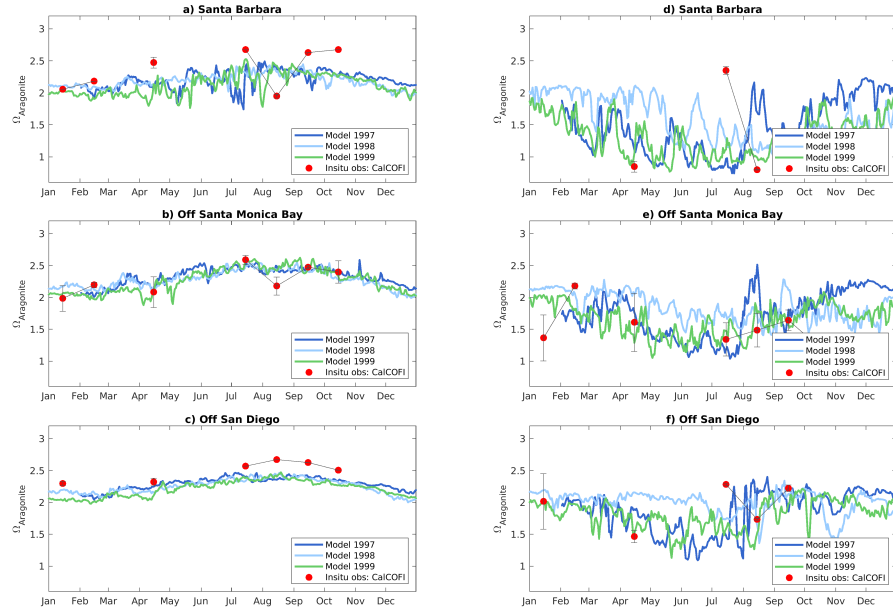Figure 19: As for Fig. 4 but for dissolved pH and (lower panel) the saturation state of aragonite.

Figure 20: Comparison of the saturation state of aragonite between different years of model output, and a climatology from CalCOFI *in situ* data. SB is near the center of Santa Barbara Channel, SM is offshore the Santa Monica Bay, and SD is offshore San Diego. Left panels show surface values, right panels values at 50 m depth.
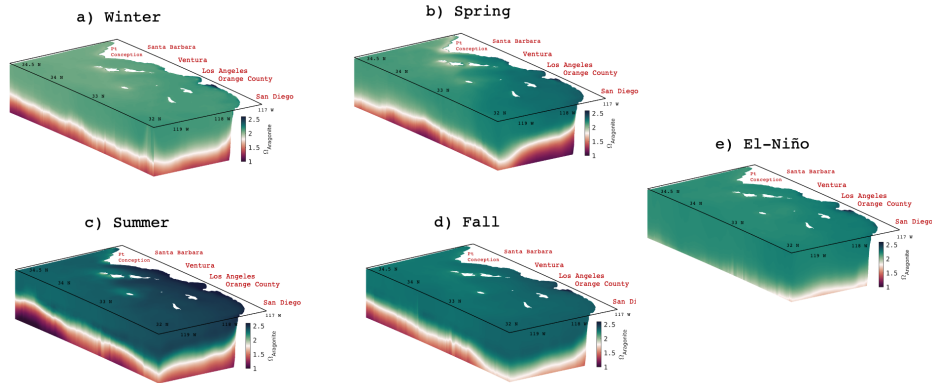

Figure 21: As for Fig. 5 but for the saturation state of aragonite.

conformity of model predictions with a rich observational dataset is a strong demonstration of model validity for coastal eutrophication applications.

Quantitative and qualitative results of confidence assessments are essential for informing management decisions, evaluating management strategies, and providing a basis for risk analyses. The most successful management approaches are those that explicitly incorporate uncertainty (e.g. Taylor, Wade, De Master, & Barlow, 2000). An assessment of model validation must consider the complex combination of model and observational uncertainties (Allen et al., 2007), including: 1) uncertainty/error in the model, including intrinsic variability; 2) uncertainty/error in measured data; 3) uncertainty from the difference in spatial scales of the model output relative to the measured data used in the comparison (specifically, comparing a 0.3 km grid cell to a discrete sampling station); and 4) uncertainty from the difference in temporal averaging of the model output relative to the measured data. For parameters in which we have high confidence in the observational record, temperature and dissolved oxygen, model performance statistics show excellent agreement for mean profiles, vertical and horizontal gradients, as well as seasonal variability. The model reproduces chlorophyll reasonably well, albeit with some bias, which can be partly attributed to measurement uncertainty, and omission of Mexican cross-border nutrient inputs. pH and ammonium have lower agreement, likely due to measurement uncertainty and sampling bias, but general spatial and temporal patterns are correctly reproduced in the model.

Greater clarity is needed in the requirements for model performance and uncertainty to support decisions on management of SCB coastal water quality and eutrophication (Boesch, 2019). These requirements are likely to be driven largely by the approach that will be used to interpret a "significant impact" (e.g. existing water quality pH and DO criteria, or biologically relevant thresholds; (Weisberg et al., 2016)), as these have significant implications for required model precision and accuracy on different spatial and and temporal scales. Future efforts to constrain uncertainty could include sensitivity analyses and model ensemble comparisons of BEC with other biogeochemical models that feature increasingly complex representations of planktonic functional groups. Finally, long-term investments are needed in coupled chemical-biological observations of phytoplankton and zooplankton community structure. These observations are critical to provide understanding of evolution of lower trophic ecosystem structure with climate change, and their relationship with biogeochemical cycles linked to OAD (Sailley et al., 2013). Ultimately, the need to constrain uncertainty will likely scale with the economic import of management decisions under consideration, which could range from increased monitoring requirements to multi-billion dollar non-point source controls and wastewater treatment plant upgrades.

References

Aita, M. N., Yamanaka, Y., & Kishi, M. J. (2007). Interdecadal variation of the lower trophic ecosystem in the northern pacific between 1948 and 2002, in a 3-d implementation of the nemuro model. *ecological modelling*, *202*(1-2), 81–94.

Alin, S. R., Feely, R. A., Dickson, A. G., Hernández-Ayón, J. M., Juranek, L. W., Ohman,

M. D., & Goericke, R. (2012). Robust empirical relationships for estimating the carbonate system in the southern california current system and application to calcofi hydrographic cruise data (2005–2011). *Journal of Geophysical Research: Oceans*, *117*(C5).

Allen, J., Somerfield, P., & Gilbert, F. (2007). Quantifying uncertainty in high-resolution coupled hydrodynamic-ecosystem models. *Journal of Marine Systems*, *64*(1-4), 3–14.

Arhonditsis, G., Tsirtsis, G., Angelidis, M., & Karydis, M. (2000). Quantification of the effects of nonpoint nutrient sources to coastal marine eutrophication: applications to a semi-enclosed gulf in the mediterranean sea. *Ecological Modelling*, *129*(2-3), 209–227.

Aumont, O., & Bopp, L. (2006). Globalizing results from ocean in situ iron fertilization studies. *Global Biogeochemical Cycles*, *20*(2).

Bednarsek, N., Feely, R. A., Howes, E. L., Hunt, B., Kessouri, F., León, P., ... others (2019). Systematic review and meta-analysis towards synthesis of thresholds of ocean acidification impacts on calcifying pteropods and interactions with warming. *Frontiers in Marine Science*, *6*, 227.

Beman, J. M., Steele, J. A., & Fuhrman, J. A. (2011). Co-occurrence patterns for abundant marine archaeal and bacterial lineages in the deep chlorophyll maximum of coastal california. *The ISME journal*, *5*(7), 1077–1085.

Boesch, D. F. (2019). Barriers and bridges in abating coastal eutrophication. *Frontiers in Marine Science*, *6*, 123.

Boesch, D. F., Brinsfield, R. B., & Magnien, R. E. (2001). Chesapeake bay eutrophication: Scientific understanding, ecosystem restoration, and challenges for agriculture. *Journal of Environmental Quality*, *30*(2), 303–320.

Bograd, S. J., Buil, M. P., Di Lorenzo, E., Castro, C. G., Schroeder, I. D., Goericke, R., ... Whitney, F. A. (2015). Changes in source waters to the southern california bight. *Deep Sea Research Part II: Topical Studies in Oceanography*, *112*, 42–52.

Booth, J., Woodson, C., Sutula, M., Micheli, F., Weisberg, S., Bograd, S., ... Crowder, L. (2014). Patterns and potential drivers of declining oxygen content along the southern california coast. *Limnology and Oceanography*, *59*(4), 1127–1138.

Brzezinski, M. A., & Washburn, L. (2011). Phytoplankton primary productivity in the santa barbara channel: Effects of wind-driven upwelling and mesoscale eddies. *Journal of Geophysical Research: Oceans*, *116*(C12).

Buitenhuis, E. T., Li, W. K., Vaulot, D., Lomas, M. W., Landry, M., Partensky, F., ... others (2012). Picophytoplankton biomass distribution in the global ocean. *Earth System Science Data*, *4*(1), 37–46.

Byun, D. W., Song, C.-K., Percell, P., Pleim, J., Otte, T., Young, J., & Mathur, R. (2006). Linkage between wrf/nmm and cmaq models. In *Presentation at 5th annual cmas conference, chapel hill, nc, available at: www. cmascenter. org* (pp. 16–18).

Capet, X., Campos, E., & Paiva, A. (2008). Submesoscale activity over the Argentinian shelf. *Geophysical Research Letters*, *35*(15).

Cederwall, H., & Elmgren, R. (1990). Biological effects of eutrophication in the baltic sea, particularly the coastal zone. *Ambio. Stockholm*, *19*(3), 109–112.

Cerco, C. F., & Cole, T. (1993). Three-dimensional eutrophication model of chesapeake bay. *Journal of Environmental Engineering*, *119*(6), 1006–1025.

Chavez, F., Pennington, J., Castro, C., Ryan, J., Michisaki, R., Schlining, B., ... Collins, C. (2002). Biological and chemical consequences of the 1997–1998 el niño in central california waters. *Progress in Oceanography*, *54*(1-4), 205–232.

Commission, O., et al. (1998). Report of the modelling workshop on eutrophication issues. 5–8 november 1996. *Den Haag, The Netherlands. OSPAR Report (86 pp.)*.

Coppola, L., Salvetat, F., Delauney, L., BSH, D. M., Karstensen, J., & Thierry, V. (2013). White paper on dissolved oxygen measurements: scientific needs and sensors accuracy. *Jerico Project*.

Cullen, J. (2001). *Primary production methods*. London, UK: Academic Press.

Dauhajre, D. P., McWilliams, J. C., & Renault, L. (2019). Nearshore lagrangian connectivity: Submesoscale influence and resolution sensitivity. *Journal of Geophysical*

846   *Research: Oceans*, *124* (7), 5180–5204.

847   Deutsch, C. A., Frenzel, H., McWilliams, J. C., Renault, L., Kessouri, F., Howard, E. M., . . .
848   Yang, S. (2020). Biogeochemical variability in the california current system. *bioRxiv*.

849   DiGiacomo, P. M., Washburn, L., Holt, B., & Jones, B. H. (2004). Coastal pollution
850   hazards in southern california observed by sar imagery: stormwater plumes, wastew-
851   ater plumes, and natural hydrocarbon seeps. *Marine Pollution Bulletin*, *49* (11-12),
852   1013–1024.

853   Dong, C., Idica, E. Y., & McWilliams, J. C. (2009). Circulation and multiple-scale variability
854   in the southern california bight. *Progress in Oceanography*, *82* (3), 168–190.

855   Fasham, M. J. (1993). Modelling the marine biota. In *The global carbon cycle* (pp. 457–504).
856   Springer.

857   Feely, R. A., Okazaki, R. R., Cai, W.-J., Bednaršek, N., Alin, S. R., Byrne, R. H., &
858   Fassbender, A. (2018). The combined effects of acidification and hypoxia on ph and
859   aragonite saturation in the coastal waters of the california current ecosystem and the
860   northern gulf of mexico. *Continental Shelf Research*, *152*, 50–60.

861   Fennel, K., & Testa, J. M. (2019). Biogeochemical controls on coastal hypoxia. *Annual*
862   *Review of Marine Science*, *11*, 105–130.

863   Foster, R. A., Kuypers, M. M., Vagner, T., Paerl, R. W., Musat, N., & Zehr, J. P. (2011).
864   Nitrogen fixation and transfer in open ocean diatom–cyanobacterial symbioses. *The*
865   *ISME journal*, *5* (9), 1484–1493.

866   Gruber, N. (2004). The dynamics of the marine nitrogen cycle and its influence on atmo-
867   spheric co 2 variations. In *The ocean carbon cycle and climate* (pp. 97–148). Springer.

868   Gruber, N., Lachkar, Z., Frenzel, H., Marchesiello, P., Münnich, M., McWilliams, J. C., . . .
869   Plattner, G.-K. (2011). Eddy-induced reduction of biological production in eastern
870   boundary upwelling systems. *Nature geoscience*, *4* (11), 787.

871   Howard, M. D., Sutula, M., Caron, D. A., Chao, Y., Farrara, J. D., Frenzel, H., . . . Sengupta,
872   A. (2014). Anthropogenic nutrient sources rival natural sources on small scales in the
873   coastal waters of the southern california bight. *Limnology and Oceanography*, *59* (1),
874   285–297.

875   Juranek, L., Feely, R., Gilbert, D., Freeland, H., & Miller, L. (2011). Real-time estima-
876   tion of ph and aragonite saturation state from argo profiling floats: Prospects for an
877   autonomous carbon observing strategy. *Geophysical Research Letters*, *38* (17).

878   Juranek, L., Feely, R., Peterson, W., Alin, S., Hales, B., Lee, K., . . . Peterson, J. (2009).
879   A novel method for determination of aragonite saturation state on the continental
880   shelf of central oregon using multi-parameter relationships with hydrographic data.
881   *Geophysical Research Letters*, *36* (24).

882   Justić, D., Rabalais, N. N., & Turner, R. E. (2005). Coupling between climate variability
883   and coastal eutrophication: evidence and outlook for the northern gulf of mexico.
884   *Journal of Sea Research*, *54* (1), 25–35.

885   Kahru, M., Kudela, R., Manzano-Sarabia, M., & Mitchell, B. G. (2009). Trends in primary
886   production in the california current detected with satellite data. *Journal of Geophysical*
887   *Research: Oceans*, *114* (C2).

888   Kang, X., Zhang, R.-H., & Wang, G. (2017). Effects of different freshwater flux repre-
889   sentations in an ocean general circulation model of the tropical pacific. *Science Bul-*
890   *letin*, *62* (5), 345 - 351. Retrieved from http://www.sciencedirect.com/science/
891   article/pii/S2095927317300932 doi: https://doi.org/10.1016/j.scib.2017.02.002

892   Kessouri, F., McLaughlin, K., Sutula, M., Ho, M., McWilliams, J., C, & Bianchi, D.
893   (2020, August). *Collection of situ monitoring data in the Southern California Bight*
894   *1950-2017 for model validation.* Zenodo. Retrieved from https://doi.org/10.5281/
895   zenodo.3988574 doi: 10.5281/zenodo.3988574

896   Kessouri, F., McWilliams, C. J., Deutsch, C., Renault, L., Frenzel, H., Bianchi, D., &
897   Molemaker, J. (2020, August). *ROMS-BEC oceanic physical and biogeochemical model*
898   *code for the Southern California Current System V2020.* Zenodo. Retrieved from
899   https://doi.org/10.5281/zenodo.3988618 doi: 10.5281/zenodo.3988618

900   Kudela, R. M., Howard, M. D., Hayashi, K., & Beck, C. (2017). Evaluation of uptake kinetics

during a wastewater diversion into nearshore coastal waters in southern california. *Estuarine, Coastal and Shelf Science*, *186*, 237–249.

Landry, M. R., Ohman, M. D., Goericke, R., Stukel, M. R., & Tsyrklevich, K. (2009). Lagrangian studies of phytoplankton growth and grazing relationships in a coastal upwelling ecosystem off southern california. *Progress in Oceanography*, *83*(1-4), 208–216.

Laufkötter, C., Vogt, M., Gruber, N., Aita-Noguchi, M., Aumont, O., Bopp, L., ... others (2015). Drivers and uncertainties of future global marine primary production in marine ecosystem models. *Biogeosciences*, *12*(23), 6955–6984.

Laurent, A., Fennel, K., Ko, D. S., & Lehrter, J. (2018). Climate change projected to exacerbate impacts of coastal eutrophication in the northern gulf of mexico. *Journal of Geophysical Research: Oceans*, *123*(5), 3408–3426.

Leinweber, A., Gruber, N., Frenzel, H., Friederich, G., & Chavez, F. (2009). Diurnal carbon cycling in the surface ocean and lower atmosphere of santa monica bay, california. *Geophysical research letters*, *36*(8).

Li, Q. P., Franks, P. J., & Landry, M. R. (2011). Microzooplankton grazing dynamics: parameterizing grazing models with dilution experiment data from the california current ecosystem. *Marine Ecology Progress Series*, *438*, 59–69.

Lucas, A. J., Dupont, C. L., Tai, V., Largier, J. L., Palenik, B., & Franks, P. J. (2011). The green ribbon: Multiscale physical control of phytoplankton productivity and community structure over a narrow continental shelf. *Limnology and Oceanography*, *56*(2), 611–626.

Lyon, G. S., & Stein, E. D. (2009). How effective has the clean water act been at reducing pollutant mass emissions to the southern california bight over the past 35 years? *Environmental monitoring and assessment*, *154*(1-4), 413.

Mantyla, A. W., Bograd, S. J., & Venrick, E. L. (2008). Patterns and controls of chlorophyll-a and primary productivity cycles in the southern california bight. *Journal of Marine Systems*, *73*(1-2), 48–60.

Maréchal, D. (2004). A soil-based approach to rainfall-runoff modelling in ungauged catchments for england and wales.

Marmorino, G. O., Smith, G. B., Miller, W. D., & Bowles, J. (2010). Detection of a buoyant coastal wastewater discharge using airborne hyperspectral and infrared imagery. *Journal of Applied Remote Sensing*, *4*(1), 043502.

McClatchie, S. (2016). *Regional fisheries oceanography of the california current system*. Springer.

McGillicuddy Jr, D. J. (2016). Mechanisms of physical-biological-biogeochemical interaction at the oceanic mesoscale.

McLaughlin, K., Dickson, A., Weisberg, S. B., Coale, K., Elrod, V., Hunter, C., ... others (2017). An evaluation of isfet sensors for coastal ph monitoring applications. *Regional Studies in Marine Science*, *12*, 11–18.

McLaughlin, K., Nezlin, N. P., Howard, M. D., Beck, C. D., Kudela, R. M., Mengel, M. J., & Robertson, G. L. (2017). Rapid nitrification of wastewater ammonium near coastal ocean outfalls, southern california, usa. *Estuarine, Coastal and Shelf Science*, *186*, 263–275.

McLaughlin, K., Nezlin, N. P., Weisberg, S. B., Dickson, A. G., Booth, J. A. T., Cash, C. L., ... others (2018). Seasonal patterns in aragonite saturation state on the southern california continental shelf. *Continental Shelf Research*, *167*, 77–86.

McWilliams, J. C. (2007). Irreducible imprecision in atmospheric and oceanic simulations. *Proceedings of the National Academy of Sciences*, *104*(21), 8709–8713.

McWilliams, J. C. (2016). Submesoscale currents in the ocean. *Proceedings of the Royal Society A: Mathematical, Physical and Engineering Sciences*, *472*(2189), 20160117.

Minna Ho, F. K. J. C. M. T. W. G., Jeroen M. Molemaker. (n.d.). High-resolution nonhydrostatic outfall plume modeling: Cross flow validation.

Moll, A., & Radach, G. (2003). Review of three-dimensional ecological modelling related to the north sea shelf system: Part 1: models and their results. *Progress in Oceanography*,

57(2), 175–217.

Montégut, C. B., Vialard, J., Shenoi, S. S., Shankar, D., Durand, F., Ethé, C., & Madec, G. (2007). Simulated seasonal and interannual variability of the mixed layer heat budget in the northern indian ocean. *Journal of Climate*, 20(13), 3249–3268.

Moore, J. K., Doney, S. C., & Lindsay, K. (2004). Upper ocean ecosystem dynamics and iron cycling in a global three-dimensional model. *Global Biogeochemical Cycles*, 18(4).

Nagai, T., Gruber, N., Frenzel, H., Lachkar, Z., McWilliams, J. C., & Plattner, G.-K. (2015). Dominant role of eddies and filaments in the offshore transport of carbon and nutrients in the California Current System. *Journal of Geophysical Research: Oceans*, 120(8), 5318–5341.

Nezlin, N. P., McLaughlin, K., Booth, J. A. T., Cash, C. L., Diehl, D. W., Davis, K. A., ... others (2018). Spatial and temporal patterns of chlorophyll concentration in the southern california bight. *Journal of Geophysical Research: Oceans*, 123(1), 231–245.

Nezlin, N. P., Sutula, M. A., Stumpf, R. P., & Sengupta, A. (2012). Phytoplankton blooms detected by seawifs along the central and southern california coast. *Journal of Geophysical Research: Oceans*, 117(C7).

Regaudie-de Gioux, A., Lasternas, S., Agustí, S., & Duarte, C. M. (2014). Comparing marine primary production estimates through different methods and development of conversion equations. *Frontiers in Marine Science*, 1, 19.

Renault, L., Hall, A., & McWilliams, J. C. (2016). Orographic shaping of us west coast wind profiles during the upwelling season. *Climate Dynamics*, 46(1-2), 273–289.

Renault, L., Masson, S., Arsouze, T., Madec, G., & McWilliams, J. C. (2020). Recipes for how to force oceanic model dynamics. *Journal of Advances in Modeling Earth Systems*, 12(2), e2019MS001715.

Renault, L., McWilliams, J. C., Jousse, A., Deutsch, C., Frenzel, H., Kessouri, F., & Chen, R. (2020). The physical structure and behavior of the california current system. *bioRxiv*.

Renault, L., Molemaker, M. J., McWilliams, J. C., Shchepetkin, A. F., Lemarié, F., Chelton, D., ... Hall, A. (2016). Modulation of wind work by oceanic current interaction with the atmosphere. *Journal of Physical Oceanography*, 46(6), 1685–1704.

Sailley, S., Vogt, M., Doney, S., Aita, M., Bopp, L., Buitenhuis, E., ... Yamanaka, Y. (2013). Comparing food web structures and dynamics across a suite of global marine ecosystem models. *Ecological Modelling*, 261, 43–57.

Savchuk, O. P., & Wulff, F. (2007). Modeling the baltic sea eutrophication in a decision support system. *AMBIO: A Journal of the Human Environment*, 36(2), 141–148.

Seegers, B. N., Birch, J. M., Marin III, R., Scholin, C. A., Caron, D. A., Seubert, E. L., ... Jones, B. H. (2015). Subsurface seeding of surface harmful algal blooms observed through the integration of autonomous gliders, moored environmental sample processors, and satellite remote sensing in southern c alifornia. *Limnology and Oceanography*, 60(3), 754–764.

Shchepetkin, A. F., & McWilliams, J. C. (2005). The regional oceanic modeling system (roms): a split-explicit, free-surface, topography-following-coordinate oceanic model. *Ocean modelling*, 9(4), 347–404.

Shchepetkin, A. F., & McWilliams, J. C. (2009). Correction and commentary for "Ocean forecasting in terrain-following coordinates: Formulation and skill assessment of the regional ocean modeling system" by Haidvogel et al., J. Comp. Phys. 227, pp. 3595–3624. *Journal of Computational Physics*, 228(24), 8985–9000.

Shchepetkin, A. F., & McWilliams, J. C. (2011). Accurate boussinesq oceanic modeling with a practical,"stiffened" equation of state. *Ocean Modelling*, 38(1-2), 41–70.

Skamarock, W. C., & Klemp, J. B. (2008). A time-split nonhydrostatic atmospheric model for weather research and forecasting applications. *Journal of Computational Physics*, 227(7), 3465–3485.

Sutton, A., Wanninkhof, R., Sabine, C., Feely, R., Cronin, M., & Weller, R. (2017). Variability and trends in surface seawater pco2 and co2 flux in the pacific ocean. *Geophysical Research Letters*, 44(11), 5627–5636.

Sutula, M., Sengupta, A., Ho, M., Kessouri, F., McLaughlin, K., McCune, K., & Bianchi, D. (2020, August). *Southern California Bight rivers, wastewater effluents and atmospheric data.* Zenodo. Retrieved from `https://doi.org/10.5281/zenodo.3981643` doi: 10.5281/zenodo.3981643

Taylor, B. L., Wade, P. R., De Master, D. P., & Barlow, J. (2000). Incorporating uncertainty into management models for marine mammals. *Conservation Biology*, *14*(5), 1243–1252.

Teel, E. N., Liu, X., Seegers, B. N., Ragan, M. A., Haskell, W. Z., Jones, B., & Levine, N. M. (2018). Contextualizing time-series data: quantification of short-term regional variability in the san pedro channel using high-resolution in situ glider data.

Terrill, E., Otero, M., Hazard, L., Conlee, D., Harlan, J., Kohut, J., . . . Lindquist, K. (2006). Data management and real-time distribution in the hf-radar national network. In *Oceans 2006* (pp. 1–6).

Todd, R. E., Rudnick, D. L., Davis, R. E., & Ohman, M. D. (2011). Underwater gliders reveal rapid arrival of el niño effects off california's coast. *Geophysical Research Letters*, *38*(3).

Uchiyama, Y., Idica, E. Y., McWilliams, J. C., & Stolzenbach, K. D. (2014). Wastewater effluent dispersal in southern california bays. *Continental Shelf Research*, *76*, 36–52.

Wanninkhof, R. (1992). Relationship between wind speed and gas exchange over the ocean. *Journal of Geophysical Research: Oceans*, *97*(C5), 7373–7382.

Warrick, J. A., DiGiacomo, P. M., Weisberg, S. B., Nezlin, N. P., Mengel, M., Jones, B. H., . . . Farnsworth, K. L. (2007). River plume patterns and dynamics within the southern california bight. *Continental Shelf Research*, *27*(19), 2427–2448.

Weisberg, S. B., Bednaršek, N., Feely, R. A., Chan, F., Boehm, A. B., Sutula, M., . . . Newton, J. A. (2016). Water quality criteria for an acidifying ocean: Challenges and opportunities for improvement. *Ocean & Coastal Management*, *126*, 31–41.

Zheng, G., & DiGiacomo, P. M. (2017). Uncertainties and applications of satellite-derived coastal water quality products. *Progress in oceanography*, *159*, 45–72.